POLITECNICO DI TORINO
Repository ISTITUZIONALE

Analytical modeling of rotor-stator potential interaction for low-speed axial fans

Original
Analytical modeling of rotor-stator potential interaction for low-speed axial fans / Bellelli, F., Arina, R., Moreau, S., Avallone, F.. - In: JOURNAL OF SOUND AND VIBRATION. - ISSN 0022-460X. - 648:(2027). [10.1016/j.jsv.2026.120196]

Availability:
This version is available at: 11583/3016882 since: 2026-10-22T14:09:44Z

Publisher:
Elsevier Science

Published
DOI:10.1016/j.jsv.2026.120196

Terms of use:

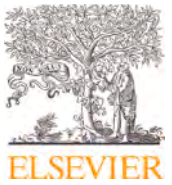
This article is made available under terms and conditions as specified in the corresponding bibliographic description in the repository

Publisher copyright

(Article begins on next page)

13 November 2026

Journal of Sound and Vibration 648 (2027) 120196



Contents lists available at ScienceDirect

Journal of Sound and Vibration

journal homepage: www.elsevier.com/locate/jsvi





Analytical modeling of rotor-stator potential interaction for low-speed axial fans

Francesco Bellelli [a,*], Renzo Arina [a], Stéphane Moreau [b], Francesco Avallone [a]

[a] Department of Mechanical and Aerospace Engineering, Politecnico di Torino, Torino, 10129, Italy
[b] Department of Mechanical Engineering, Université de Sherbrooke, Sherbrooke, Québec, Canada

ARTICLE INFO

Keywords:
Aeroacoustics
Axial fan
Potential flow
Analytical model
Tonal noise
Rotor-stator interaction
Multi-fidelity

ABSTRACT

This paper presents an analytical model to predict tonal noise of rotor-stator potential interaction for low-speed axial fans. The model is validated against high-fidelity lattice-Boltzmann (LBM) simulations for two fan configurations, varying the blades and vanes azimuthal spacing. The model couples Blade Element Momentum Theory, for steady blade loading, with an unsteady Sears-based formulation for unsteady blade loading. The latter is enhanced with a modification of the chordwise pressure distribution function to eliminate the leading edge singularity. The velocity field at the blade trailing edge is reconstructed via potential flow using two novel approaches: a Gaussian velocity deficit and a cascade representation of stator vanes. Results show that the modified pressure function improves the agreement with the surface pressure distribution obtained from LBM at the leading edge; moreover, the proposed flow-field reconstructions reproduce the dominant velocity features and the tonal noise trends reasonably compared with the LBM results. The model is found to capture the effect of blade-vane phasing on tonal noise generation and to reproduce the main characteristics of the acoustic directivity pattern. Remaining discrepancies in broadband noise indicate the need of including trailing edge and tip noise models.

1. Introduction

Fan noise is a critical concern for manufacturers due to increasingly stringent regulations; the transition from thermal to electric propulsion is making this noise source dominant. For this reason, it is necessary to simultaneously optimize aerodynamic and aeroacoustics performances in early stages of the design. However, high-fidelity CFD simulations are often computationally unfeasible at the design phase. Therefore, analytical and reduced-order models are crucial to ensure an efficient and feasible design process [1].

Several noise sources are present in a cooling fan. Monopole (thickness) and dipole (loading) noise sources, caused by the air displacement due to the blade passage and the rotating force are usually dominant. In contrast, quadrupole noise sources are negligible at the low Mach number at which they operate [2]. Loading noise can be split into steady and unsteady loading noise. The former characterizes the noise spectrum with narrowband peaks at frequencies multiple of the Blade Passing Frequency (BPF), defined as $BPF = \Omega B$, in the hypothesis of azimuthally evenly spaced blades. If the blades are not evenly spaced, additional peaks at subharmonic frequencies are present. The steady loading noise was first investigated by Gutin [3] and later by Lowson [4,5] and Hanson [6–9]. However, Sharland [2] showed that, when present, the unsteady component of loading noise outweighs the steady one.

* Corresponding author.
E-mail address: francesco.bellelli@polito.it (F. Bellelli).

https://doi.org/10.1016/j.jsv.2026.120196
Received 16 December 2025; Received in revised form 10 September 2026; Accepted 13 October 2026
Available online 14 October 2026
0022-460X/© 2026 The Author(s). Published by Elsevier Ltd. This is an open access article under the CC BY license (http://creativecommons.org/licenses/by/4.0/).

Nomenclature

CFD	Computational Fluid Dynamics
RANS	Reynolds Averaged Navier Stokes
LBM	Lattice-Boltzmann Method
FW-H	Ffowcs-Williams and Hawkings
BEMT	Blade Element Momentum Theory
VR	Variable Resolution
EB/EV	Evenly spaced blades and evenly spaced vanes
UB/UV	Unevenly spaced blades and unevenly spaced vanes
PS, SS	Pressure Side, Suction Side
$\tilde{q}$	Quantity q in the frequency domain
vox	Number of voxels in the finest VR region [-]
B, V	Number of rotor blades and stator vanes [-]
x, y, z	Axial, horizontal, and vertical coordinates [m]
$R = \sqrt{y^2 + z^2}$	Radial position in the yz plane [m]
$\theta = \tan^{-1}\left(\frac{z}{y}\right)$	Azimuthal position in the yz plane [°]
r_1	Probe radius in the xy plane [m]
φ	Probe angle in the xy plane with respect to the x axis [°]
Ψ	Probe angle in the xz plane with respect to the x axis [°]
x_1^*	Non-dimensional chordwise coordinate [-]
N_s, N_c	Number of spanwise and chordwise points [-]
D, D_h	Fan tip and hub diameters [m]
R_t, R_h	Fan tip and hub radii [m]
c	Fan tip chord [m]
t_c	Fan tip clearance [m]
s	Rotor-stator axial separation [m]
γ	Twist angle [°]
u, v_r, v_θ	Axial, radial, and tangential velocity components [m/s]
V_∞	Inflow velocity [m/s]
v	Upwash velocity [m/s]
Ω	Fan rotational frequency [Hz]
p	Static pressure [Pa]
ρ	Density [kg/m^3]
ν	Kinematic viscosity [m^{2}s]
$v_{tip} = \Omega R_t$	Tip velocity [m/s]
$p^\circ_{tip} = \frac{1}{2}\rho v_{tip}^2$	Tip dynamic pressure [Pa]
$Re_c = \frac{v_{tip}c}{\nu}$	Tip chord-based Reynolds number [-]
$c_p = \frac{p - p_{amb}}{p^\circ_{tip}}$	Pressure coefficient [-]
T	Fan thrust [N]
Q	Fan aerodynamic torque [Nm]
$\Delta p = p_{amb} - p$	Fan pressure rise [Pa]
$\dot{V}$	Volume flow rate through the fan [m^3/s]
$\psi = \frac{2\Delta p}{\rho v_{tip}^2}$	Load coefficient [-]
$\phi_f = \frac{4\dot{V}}{\pi(D^2 - D_{hub}^2)v_{tip}}$	Flow coefficient [-]
c_0	Sound speed [m/s]
f	Frequency [Hz]
λ	Wavelength [m]
$\mathrm{BPF} = B\Omega$	Blade Passing Frequency [Hz]
$\mathrm{SPL} = 20\log_{10}\left(\frac{p_{rms}}{2\cdot 10^{-5}}\right)$	Sound Pressure Level [dB]
$\mathrm{OASPL} = 10\log_{10}\left(\sum_i 10^{\frac{SPL(f_i)}{10}}\right)$	Overall Sound Pressure Level [dB]

In addition to rotor only tones, tonal peaks can arise from rotor-stator interaction. In these configurations, three main mechanisms can be distinguished [10]. First, the viscous wakes shed by the rotor blades impinge on the downstream stator vanes, producing periodic fluctuations of the stator loading. Second, the stator vanes can interact with the potential field of the rotor that propagates downstream, although this contribution is generally weaker than the wake-induced interaction. Third, the rotor blades can periodically

interact with the potential field associated with the stator leading edges that propagates upstream, thereby producing unsteady rotor loading. The relative importance of these mechanisms depends strongly on the rotor-stator spacing; in particular, potential-field interactions become increasingly important as the axial spacing is reduced, as shown by Wu et al. [11] both numerically and experimentally.

Another source of blade loading unsteadiness is when a turbulent flow impinges on the blades. This gives rise to the so-called turbulent ingestion noise. It is typically dominant at low frequency and can increase both the broadband and tonal noise, depending on the turbulent vortex structures topology. Sanjosé and Moreau [12] used an approach based on Amiet leading edge noise model [13], with the formulation of Sinayoko et al. [14,15], to compute turbulent ingestion noise in an axial fan. They fed the model with isotropic von Kàrmàn and Liepmann turbulence spectra computed with the aid of RANS simulations. They were able to obtain accurate results at low fan flow rates up to the design point, while consistently underestimating the total Sound Power Level (SWL) at higher flow rates. Dieste and Gabard [16] applied instead a Random Particle Mesh (RPM) method to generate a synthetic turbulent field including non-Gaussian filters to obtain more realistic energy spectra. They validated the results against the conventional Amiet [13] formulation and obtained encouraging predictions of turbulence energy spectra using the RPM rather than conventional models such as von Kàrmàn and Liepmann.

Since tonal noise is known to be more annoying than broadband noise, particular relevance shall be given to the development of analytical models aimed at quickly predicting and optimizing this noise source. For instance, Wu et al. [17], Daydé-Thomas et al. [18], and Rendon et al. [19] calculated far-field tonal noise by sampling the loading from unsteady simulations. However, during the design phase this approach is computationally expensive as the only speed-up with respect to conventional hybrid Computational Aeroacoustics (CAA) approaches is on the acoustic propagation part. To circumvent this flaw, Tannoury [20] compared different acoustic mesh resolutions and dipole phase summation approaches to obtain the far-field noise of an engine cooling fan. It has been found that axial, radial and azimuthal phase lags are important only at lateral microphone positions. To reduce the computational cost of the unsteady blade loading calculation, Caro and Moreau [21] proposed a wake-interaction noise model based on Sears' unsteady aerodynamic theory [22]. They found close agreement with experimental results on noise radiation when the Sears' model was fed with experimental inlet velocity fluctuations. More recently, Yunus et al. [23] used two different methodologies, based respectively on the Sears' model and on an unsteady extension of the BEMT approach [24], to predict the unsteady loading from a time-averaged non-uniform flow field upstream of the blades. Both approaches resulted in sufficiently accurate tonal noise predictions. Moreover, Soulat et al. [25] used RANS simulations of a single blade passage to compute wake-induced interaction noise on a tandem contra-rotating rotor configuration with an approach based on Sears' model, increasing the computational efficiency of the aerodynamic calculations. Guerin et al. [26] and Grasso et al. [27] used RANS simulations to further reduce the computational cost of the flow field calculation. Their results showed that it is possible to predict rotor-stator interaction noise by propagating in the far-field the unsteady blade loading computed with Sears' model fed with RANS velocity profiles.

The aforementioned works focused on the blade loading fluctuations induced by upstream obstacles. However, Canepa et al. [28] showed that, for engine cooling fans with small rotor-stator axial separation, the potential effect of the stator vanes on the rotor blades is a primary tonal noise source that outweighs the contribution from the impingement of the rotor wake on the stator vanes. On the analytical side, only a few attempts have been made to model such noise source for open rotors. Vella et al. [29,30] used potential flow theory, to model the flow field near the blade, combined with Sears' model [22] for unsteady blade loading and Hanson model for far-field noise propagation, leading to sufficiently fast and accurate acoustic results. Similarly, Zamponi et al. [31] proposed a low cost analytical framework for potential interaction tonal noise in generic propeller-strut arrangements, using potential flow modeling and conformal mapping to handle non circular strut cross sections with sufficient accuracy. Moreover, SanjosÃ© et al. [32,33] computed the rotor-stator potential interaction noise on the NASA ANCF rig using Parry's model [34] to predict the unsteady blade loading in the frequency domain and classic potential flow theory to predict the flow field at the trailing edge. Their results compare well with high-fidelity numerical simulations, showing that two-dimensional inviscid theory is sufficient to obtain the main trends of the potential excitation affecting the rotor. They also showed that it is equivalent to use Parry's approach or the reversed Sears' method proposed by Roger et al. [35] if the Kutta condition is imposed at the trailing edge. He et al. [36] also proposed an analytical estimate of the rotor and strut loading using Parry's model and a set of infinite cascades for both rotor and stator sections, showing close agreement with measurements. They also highlighted that the relative contributions of rotor and strut sources depend on blade spacing and observer position.

This paper presents the development and validation of an analytical aeroacoustic model. The model is able to predict, in addition to the blade induced unsteady loading noise, the rotor-stator potential interaction tonal noise. The proposed model can use as inputs an analytical solution of the flow field at the blade leading and trailing edges or a RANS simulation with periodic boundary conditions, thus relying only on low computational cost fluid dynamic calculations. The results from the model are compared against high-fidelity CFD simulations based on the lattice-Boltzmann method (LBM) on two different fan configurations with varying rotor blades and stator vanes azimuthal spacing. This work is an extension of the previous work by Bellelli et al. [37], which did not include the analytical approach to reconstruct the velocity flow field, rather focusing on the unsteady loading noise prediction by means of RANS simulations. This work is a further step towards the development of an acoustic optimization framework for the complete cooling module geometry in installed conditions.

The remainder of the paper is structured as follows: Section 2 describes the reference fan geometry, Section 3 details the analytical model, and Section 4 outlines the numerical setup for the high-fidelity CFD simulations used as comparison and of the RANS simulations. LBM simulations are analyzed in Section 5, in order to define the main noise sources, while the results obtained with the analytical model are discussed in Section 6. Finally, main conclusions are presented in Section 7.

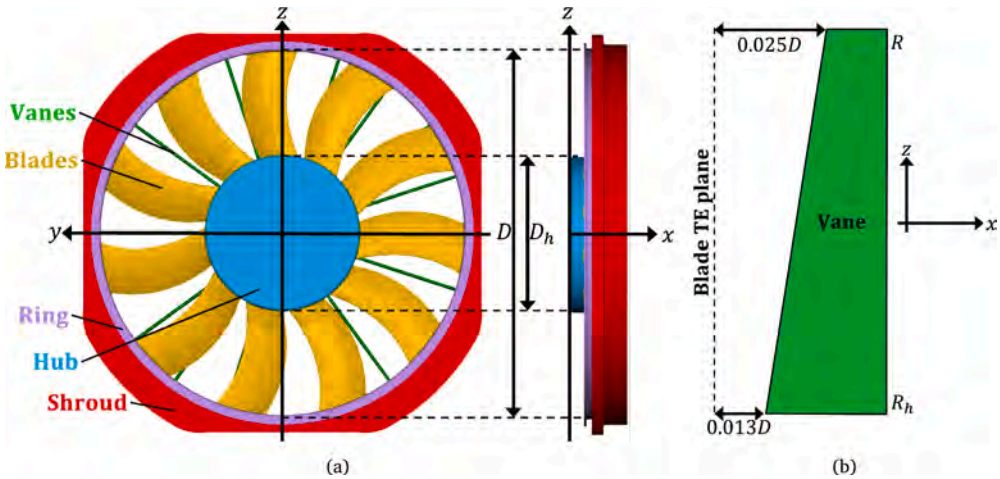


Fig. 1. Reference engine cooling fan. The main parts of the system are shown with different colors. (a): Cooling fan. (b): Sketch of a stator vane at $y/D = 0$. (For interpretation of the references to color in this figure legend, the reader is referred to the web version of this article.)

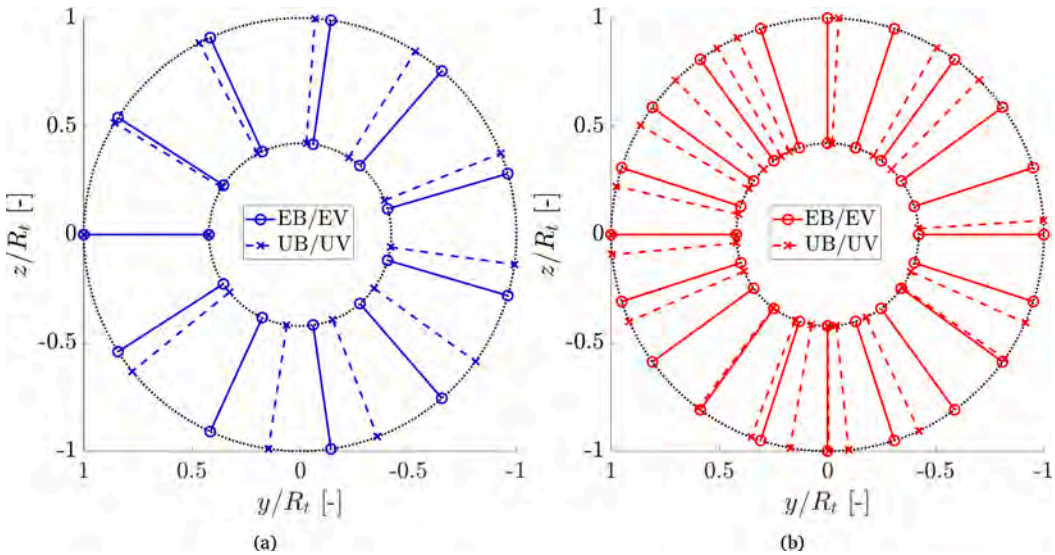


Fig. 2. Sketch of the angular position of the EB/EV and UB/UV configurations in the yz plane. (a): Rotor blades. (b): Stator vanes.

2. Geometry

The engine cooling module consists of a rotor and a stator, as shown in Fig. 1a. The rotor has $B = 11$ identical blades connected to a hub at the root and to a ring at the tip. The rotor diameter is $D = 0.465$ m and the hub-tip ratio is $D_h/D = 0.42$. The chord at the tip is $c/D = 0.14$ and the tip clearance is $t_c/D = 0.0086$. The rotor blades are swept in the yz plane, as visible in Fig. 1a. The stator has $V = 20$ identical vanes, connected to a shroud, skewed in the xz plane, as shown in Fig. 1b; therefore, the rotor-stator axial separation varies from $s/D = 0.013$ at the hub to $s/D = 0.025$ at the tip. It should be noted that the vane skew is obtained by decreasing the vane chord from the hub to the tip, while keeping fixed the trailing edge position (Fig. 1b). This geometry is a simplified version of the one used by Bellelli et al. [38] in a previous study. Since the fan is an industrial product subject to confidentiality restrictions, results are reported using non-dimensional parameters. Moreover, the results reported in Section 6 are shown omitting absolute dB levels.

In order to assess the model capability to predict the SPL variations at discrete frequencies, two different configurations have been numerically investigated. The first configuration (EB/EV) is characterized by an even azimuthal spacing of both blades and vanes, while the second configuration (UB/UV) is characterized by an uneven azimuthal spacing of both blades and vanes. The UB/UV configuration has been obtained by randomly perturbing the angular position of blades and vanes of the EB/EV configuration at the hub with an approach similar to the one described by Cattanei et al. [39], bounding the minimum and maximum

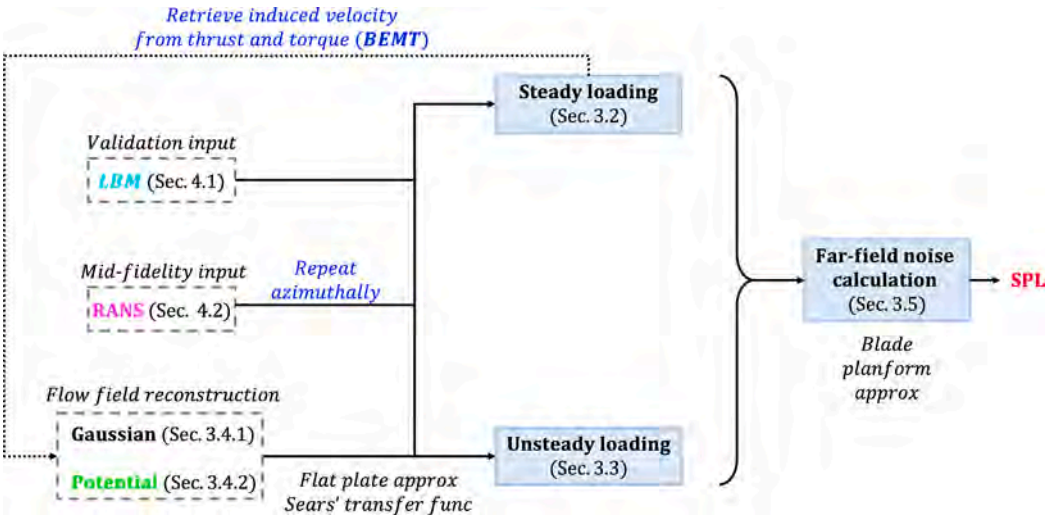


Fig. 3. Flowchart of the analytical model. The LBM input is shown in italics because it is included only for validation purposes in this paper.

azimuthal spacing between two consecutive elements respectively to the 25% and the 140% of the evenly spaced configuration. A schematic representation of the azimuthal distribution of rotor blades and stator vanes for the two configurations is provided in Fig. 2a and b.

The fan operates at free blowing conditions (i.e., $\psi = \frac{2\Delta p}{\rho U_{tip}^2} = 0$), resulting in a volume flow rate coefficient of $\phi_f = \frac{4\dot{V}}{\pi(D^2 - D_{hub}^2)v_{tip}} = 0.19$ at a rotational frequency of the fan $\Omega = 50.8$ Hz. The resulting Reynolds number based on the chord at the tip is $Re_c = 3.2 \cdot 10^5$, and the tip Mach number is $M_t = 0.22$. The reason for the choice of this operating point is twofold: firstly, the free blowing condition is often considered a standard in the acoustic tests by manufacturers; secondly, the proposed approach, as will be shown in Section 3, currently relies on the BEMT, which does not consider the presence of a pressure rise.

3. Analytical model

A flowchart of the analytical model implementation is shown in Fig. 3. Both the steady and unsteady loading noise are computed using a frequency domain rotating dipole approach. In both steady and unsteady loading calculations. Data from LBM have been used for validation purposes. For this reason, Fig. 3 shows the "LBM" label in italics. The LBM simulations provide a high-fidelity aeroacoustic reference solution for the validation of the analytical model. Although the latter is specifically focused on tonal noise prediction, the use of LBM enables the direct computation of the acoustic fluctuations, avoiding additional assumptions associated with hybrid approaches, due to its intrinsic compressible nature. As a matter of fact, the LBM lower numerical dispersion and dissipation with respect to conventional Navier-Stokes solvers allow for a direct computation of the aeroacoustic field up to frequencies corresponding to 15 voxels per wavelength [40].

The model can be fed in different ways, spanning different fidelity levels:

1. The steady loading can be obtained from time-averaged results provided by:
   - RANS;
   - BEMT, as it will be described in Section 3.2.

   Although RANS simulations can provide the mean aerodynamic loading of the fan with satisfactory accuracy, their computational cost remains significant when repeated evaluations are required, as will be reported in Section 6. The adoption of BEMT is therefore motivated by the objective of developing a computationally efficient reduced-order framework suitable for rapid aeroacoustic predictions and future design space exploration or optimization procedures, requiring a large number of model evaluations.
2. For the unsteady loading calculations, the azimuthal distribution of the upwash velocity field is needed to feed Sears' model as it will be described in Section 3.3. The upwash velocity field is first expressed in the stationary reference frame as a function of the circumferential coordinate θ and spanwise position R. Since the rotor crosses this periodically distorted field, the circumferential spatial harmonics in the stationary reference frame are perceived by each blade as unsteady loading at a frequency $f = w\Omega$. Accordingly, the azimuthal Fourier coefficients are directly used as the blade harmonic excitation in the Sears' model. The resulting unsteady blade loading harmonics are subsequently introduced into the rotating dipole formulation, where factors involving the instantaneous blade azimuth account for the transformation of each rotating source back into the stationary observer frame and for the relative inter-blade phase. The upwash velocity field can be:
   - sampled from RANS simulations;
   - obtained with two different analytical approaches described in Section 3.4.

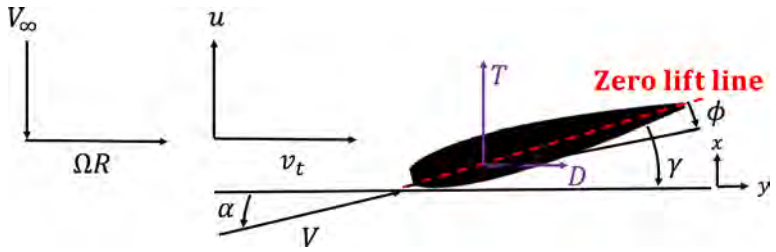


Fig. 4. Schematic view of the generic blade section used in the BEMT calculation.

For this purpose, time-averaged velocity flow fields at $0.0075D$ upstream of the blade leading edge and downstream of the trailing edge have been extracted and averaged in the fixed reference frame. For the LBM simulations, the average has been done on the last 10 revolutions and the sampling planes positioning have been chosen to lie immediately outside the sliding mesh region. For the RANS simulations, the velocity field has been azimuthally repeated according to the angular position of the stator vanes shown in Fig. 2b, to reconstruct the full velocity field from the periodic sectional domain. To fill the regions outside of the single blade passage sampling domain, a spline-based interpolation between the boundaries of neighboring subdomains has been made. The sampling plane location is the same for all the simulations to ensure consistency. Although the instantaneous flow field downstream the rotor contains both the rotor wake and the vane-induced potential disturbance, the flow quantities used as input for Sears' model were obtained through time-averaging in the stationary reference frame. The averaging procedure filters out the rotor wake contribution due to its phase-varying nature in the stationary frame, whereas the vane-induced potential field remains stationary and is therefore preserved. As a result, the extracted forcing field predominantly represents the stator-induced potential disturbance employed in the analytical model. Hence, throughout the reminder of the paper, the authors will always refer to the potential field generated by the stator vanes.

The model was implemented in MATLAB and run on an Intel i9-10900X 4.50 GHz Dell Precision 5820 X-Series workstation. The average computational cost is between 0.025 and 0.25 CPU hours, depending on the time-averaged flow field input. The computational cost did not include the computational cost of LBM and RANS simulations.

3.1. Blade discretization

Each blade is discretized in N_s points in the spanwise direction and N_c points in the chordwise direction. The minimum values for N_s and N_c should be chosen so that the resulting length of each spanwise and chordwise segment is acoustically compact, i.e., $L \leq \lambda$, where $\lambda = c_0/f$ is the wavelength and L is the length of each segment in the spanwise or chordwise direction. Nevertheless, a convergence study on both N_s and N_c has been performed as reported in Appendix C. For each spanwise position R, the chord $c(R)$ and twist $\gamma(R)$ distributions are extracted from the fan CAD, together with information on the sectional airfoil shape, the segment azimuthal phase, and the rotor to stator axial spacing.

3.2. Steady loading

A sketch of the generic blade section is provided in Fig. 4. For each spanwise position R, the sectional thrust and torque are calculated following both the momentum theory and the blade element theory assuming a uniform axial inflow with velocity V_∞, leading to the following identities

$$\begin{cases} \frac{dT}{dR} = 4\pi R\rho V_\infty^2(1+a)a = B\frac{1}{2}\rho V_1^2 c(c_l\cos\phi - c_d\sin\phi), \\ \frac{dQ}{dR} = 4\pi R^2\rho V_\infty^2\Omega R(1+a)b = B\frac{1}{2}\rho V_1^2 c(c_l\sin\phi + c_d\cos\phi)R, \end{cases} \tag{1}$$

where $a = u/V_\infty - 1$ is the axial velocity induction coefficient, $b = 1 - v_t/(\Omega R)$ is the tangential velocity induction coefficient, $\phi = \gamma - \alpha$ is the inflow angle, α is the angle of attack of the blade section, $V_1 = \sqrt{u^2 + v_t^2}$ is the total velocity at each radial section, and $M = \Omega R/c_0$ is the Mach number. The lift coefficient $c_l(\alpha, Re_c, M)$ and drag coefficient $c_d(\alpha, Re_c, M)$ of the sectional airfoil are calculated by interpolating a predefined polar database, computed by means of XFOIL [41]. Starting from a tentative value, the axial and tangential velocity induction factors are iteratively calculated from Eq. (1) until convergence. The Prandtl-Glauert compressibility correction factor

$$C = \frac{1}{\sqrt{1-M^2} - \frac{M^2}{1+\sqrt{1-M^2}}\frac{||c_l||}{2}}, \tag{2}$$

is applied to the lift coefficient c_l. It is worth to note that XFOIL is ran without the Karman-Tsien compressibility correction. The Prandtl-Glauert one is preferred to improve XFOIL convergence.

The hub and tip losses are considered by introducing the correction factor [42]

$$F_{ht} = \left(\frac{2}{\pi}\right)^2 \exp\left(-\frac{B}{2}\sqrt{1+\left(\frac{\Omega R^2}{V_\infty(1+a)}\right)^2}\frac{R_t - R_h}{R}\right) \tag{3}$$

to the thrust and torque spanwise distributions.

3.3. Unsteady loading

The unsteady component of the force acting on each strip at a frequency $f = w\Omega$, with $w \in \mathbb{Z}$, is computed with Sears' model [22], based on the flat plate and one-dimensional gust approximations, as

$$\tilde{F}(w, x_1^*, R) = \int_{r_I}^{r_O}\int_{c_I}^{c_O} c(R)\rho\Omega R\tilde{v}(w, R)S(\sigma_\theta)\sqrt{\frac{1-x_1^*}{1+x_1^*}}\,dx_1^*\,dR, \tag{4}$$

where $c(R)$ is the blade chord at the spanwise location R, $\sigma_\theta = (fc/2)/(\Omega R) = (wc)/(2R)$ is the dimensionless gust frequency, ρ is the air density, $\tilde{v}(w, R)$ is the azimuthal Fourier transform of the upwash velocity at a frequency f and spanwise position R, $x_1^* = 2x/c - 1$ is the non-dimensional chordwise coordinate, and $S(\sigma_\theta)$ is Sears' transfer function. Its original formulation is

$$S_0(\sigma_\theta) = \frac{1}{i\sigma_\theta\left[K_0(i\sigma_\theta) + K_1(i\sigma_\theta)\right]}, \tag{5}$$

where $K_0(x)$ and $K_1(x)$ are respectively the zero-th and first order Bessel functions of the second kind. In order to improve the accuracy of Sears' model, two modifications are introduced in Eq. (4). The first modification involves the Sears' function. Eq. (5) is expanded to consider compressibility effects [43] as well as blade angle of attack and camber [44,45]. Therefore, the transfer function used in the present work is

$$S(\sigma_\theta) = S_\beta(\sigma_\theta) + \gamma(R)S_\alpha(\sigma_\theta) + y_c^{max}(R)S_c(\sigma_\theta), \tag{6}$$

where $y_c^{\max}(R)$ is the maximum camber of the airfoil at each spanwise section. The compressibility effect is considered in the $S_\beta(\sigma_\theta)$ term, the blade angle of attack effect is included in the $S_\alpha(\sigma_\theta)$ term, and the blade camber effect is considered in the $S_c(\sigma_\theta)$ term. The complete expressions of these terms are reported in Appendix A.

Eq. (4) is integrated in the spanwise and chordwise directions within the inner and outer radii (r_I, r_O) and chordwise sections (c_I, c_O). Then, the values of $\tilde{T} = \tilde{F}\cos\gamma$ and $\tilde{\Theta} = \tilde{F}\sin\gamma$ are calculated from $\tilde{F}$ by knowing the blade twist angle γ at each spanwise position.

The second modification involves the square root term

$$f(x_1^*) = \sqrt{\frac{1-x_1^*}{1+x_1^*}}, \tag{7}$$

which models the pressure distribution in the chordwise direction. Such function has a $+\infty$ singularity at the leading edge ($x_1^* = -1$) and is zero at the trailing edge ($x_1^* = 1$), being the characteristic chordwise pressure distribution on a flat plate. To provide a more realistic approximation of the chordwise loading distribution of a finite thickness airfoil while retaining the original Sears' analytical framework, the following modified function $f_m(x_1^*)$ is proposed in lieu of $f(x_1^*)$:

$$f_m(x_1^*) = \sqrt{A\exp(x_1^{*2})\frac{1-x_1^*}{(1+x_1^*)^{-B}}}, \tag{8}$$

where A is a parameter that is calculated so that the integral

$$\int_{-1}^{1} f_m(x_1^*)dx = \int_{-1}^{1} f(x_1^*)dx = \pi \tag{9}$$

is preserved. The parameter B is calculated so that $f_m(x_1^*)$ has its maximum at the x_1^* location corresponding to the location of the suction peak in the c_p chordwise distribution of the blade airfoil. The accuracy of this modification is assessed in Appendix D. It should be noted that the proposed modification does not constitute a reformulation of Sears' boundary value problem. The original transfer function is retained, and the modified chordwise weighting should be interpreted as a regularization to mitigate the leading edge singularity and improve the representation of finite airfoil loading effects.

Eq. (4) is fed with the time-averaged flow fields. The upwash velocity component is sampled at the blade leading and trailing edge as described in Section 3. The flow field at the leading edge provides information on the interaction between the rotor and the non-uniform inflow resulting from upstream flow distortions. On the other hand, the flow field at the trailing edge provides information on the rotor-stator potential interaction. For this latter mechanism, the disturbance originates downstream of the rotor and propagates upstream toward the rotor blade. This configuration is opposite to the one conventionally adopted in Sears' problem, in which an incident gust is convected from the leading edge toward the trailing edge. The reversed Sears' approach proposed by Roger et al. [35,46] is therefore adopted. In this formulation, the airfoil response is evaluated for a disturbance acting from the trailing edge side of the blade, allowing the Fourier components of the potential disturbance propagating upstream to be related to the resulting unsteady blade loading. This approach has also been adopted by Vella et al. [29] for the analytical prediction of mutual rotor-stator interaction noise.

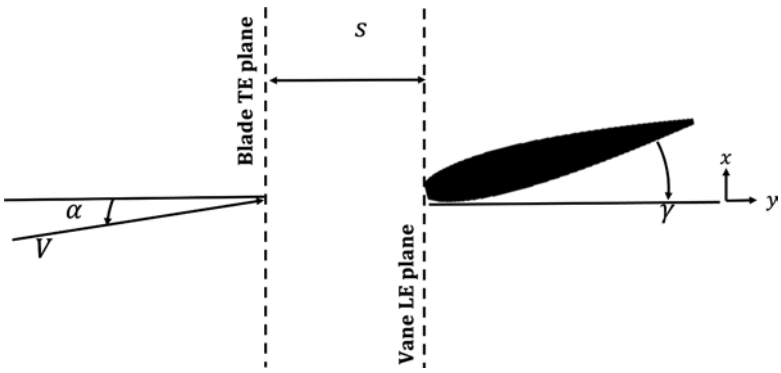


Fig. 5. Sketch of the classic 2D potential flow calculation on an isolated Joukowski profile.

3.4. Analytical 2D models under potential flow assumptions

Two analytical approaches are proposed to predict the time-averaged flow field at the blade leading and trailing edges used as input for Sears' model.

3.4.1. Gaussian velocity deficit

The first approach consists in assuming that the upwash velocity deficit resulting from the presence of an upstream or downstream obstruction can be modeled with a Gaussian function. It is aimed at providing a smooth reconstruction kernel to represent the characteristic spatial extent of the velocity deficit while ensuring a continuous and periodic circumferential forcing distribution suitable for the Fourier decomposition required by Sears' model.

The resulting upwash velocity field at the blade leading edge or trailing edge can be calculated as

$$v(\theta) = 1 - \sum_{i=1}^{N_{obstr}} \exp\left[-\left(\frac{\theta-\theta_i}{\Delta\theta_i}\right)^2\right], \tag{10}$$

where θ indicates the azimuthal coordinate, $\Delta\theta$ indicates the azimuthal thickness of the obstruction, the index i identifies the generic ith obstruction, and N_{obstr} is the number of upstream or downstream obstructions. However, Eq. (10) is not correctly scaled, as it is bounded between 0 and 1. Therefore, $v(\theta)$ should be scaled at each spanwise location R.

Regarding the downstream flow field, $v(\theta)$ is scaled with respect to the azimuthal maximum and minimum values of the upwash velocity as

$$v(\theta, R) = \left\{1 - \sum_{i=1}^{N_{obstr}} \exp\left[-\left(\frac{\theta-\theta_i}{\Delta\theta_i}\right)^2\right]\right\}\left[v_{\max,\theta}(R) - v_{\min,\theta}(R)\right] + v_{\min,\theta}(R). \tag{11}$$

To compute $v_{\max,\theta}(R)$ and $v_{\min,\theta}(R)$ for the downstream flow field, the 2D inviscid velocity field is calculated in the vicinity of a Joukowski airfoil, invested by a uniform flow with velocity

$$V(R) = \sqrt{V_{iA}(R)^2 + V_{iT}(R)^2} \tag{12}$$

and angle of attack

$$\alpha(R) = \tan^{-1}\frac{V_{iT}(R)}{V_{iA}(R)}, \tag{13}$$

by means of the classic potential flow theory with conformal mapping [47]. In this context, the effect of the stator loading and angle of attack is implicitly included through the spanwise scaling quantities $v_{\max,\theta}(R)$ and $v_{\min,\theta}(R)$. The velocity components in Eqs. (12) and (13) are the axial and tangential induced velocity components that can be calculated with the momentum theory as

$$V_{iA}(R) = \sqrt{\frac{1}{4\pi\rho R}\frac{dT}{dR}(R)} \tag{14}$$

and

$$V_{iT}(R) = \frac{1}{4\pi\rho R^2 V_{iA}(R)}\frac{dQ}{dR}(R). \tag{15}$$

The velocity field is sampled at a distance s from the vane leading edge so that the value at the blade trailing edge can be obtained, as sketched in Fig. 5; hence, $v_{min,\theta}(R)$ and $v_{max,\theta}(R)$ are computed respectively as the minimum and maximum values of the velocity field along the sampling line. The chord $c_v(R)$, maximum thickness $y^{\max}_{th,v}(R)$, and twist angle $\gamma_v(R)$ of the Joukowski airfoil are calculated so that they match the chord, maximum thickness and twist angle of the stator vanes. However, the classic potential

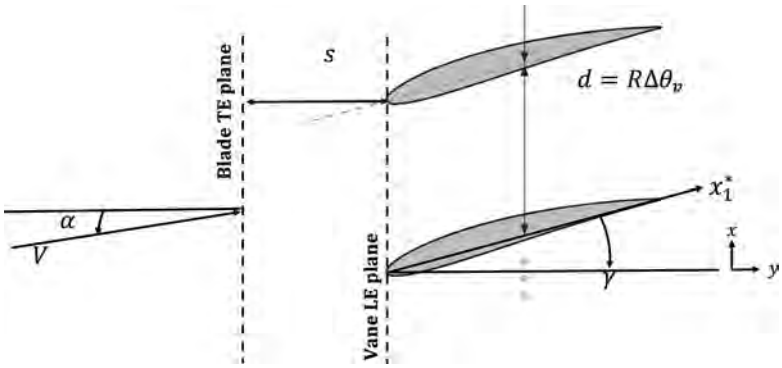


Fig. 6. Sketch of the 2D potential flow calculation of an infinite cascade of airfoils.

flow theory assumes an isolated Joukowski airfoil, therefore neither including eventual cascade effects nor allowing to consider the airfoil shape.

Concerning the potential distortion generated by an upstream obstruction, this is not modeled with an analytical approach. The Gaussian distribution in Eq. 10 is only used to prescribe the azimuthal shape and characteristic width of the disturbance, whereas its amplitude is determined semi-empirically. In particular, at each spanwise location, the characteristic amplitude of the velocity perturbation is assumed to be a fraction of the local reference velocity $V(R)$, using a prescribed dimensionless coefficient. In the present case, the only potential distortion taking place upstream is the one induced by the four cuts on the shroud seen in Fig. 1a; the amplitude of the distortion has been obtained through a fit of the LBM time-averaged flow field, yielding a dimensionless coefficient of 0.01 with which $V(R)$ has been scaled for $R/R_{tip} \geq 0.8$.

3.4.2. Airfoil cascade

To consider the vane airfoil and to account for possible cascade effects occurring among neighboring vanes, a second approach is proposed. The benefits of this approach, rather than an isolated airfoil solution, are further discussed in Appendix B. The 2D inviscid velocity field in the vicinity of an infinite airfoil cascade is computed as proposed by Baddoo and Ayton [48] and sketched in Fig. 6. The complex velocity perturbation to the unitary undisturbed flow field $\Phi(z) = v_x(z) - iv_y(z)$, with $z = x + iy$ can be calculated as

$$\begin{aligned}\Phi(z) =& \mathrm{i}\alpha\left(1 - \exp\left(\frac{-\pi}{d}\right)\sqrt{\frac{\sinh\left(\pi\dfrac{z-\exp(\mathrm{i}\gamma)}{d}\right)}{\sinh\left(\pi\dfrac{z+\exp(\mathrm{i}\gamma)}{d}\right)}}\right)\\ &-\frac{1}{d}\int_{-1}^{1} y'_{\mathrm{th,v}}(\tau)\coth\left(\frac{\pi(\tau\exp(\mathrm{i}\gamma)-z)}{d}\right)\exp(\mathrm{i}\gamma)\,\mathrm{d}\tau\\ &-\frac{1}{\mathrm{i}}\sqrt{\frac{\sinh\left(\pi\dfrac{z-\exp(\mathrm{i}\gamma)}{d}\right)}{\sinh\left(\pi\dfrac{z+\exp(\mathrm{i}\gamma)}{d}\right)}}\\ &\int_{-1}^{1} y'_{\mathrm{c,v}}(\tau)\sqrt{\frac{\sinh\dfrac{\exp(\mathrm{i}\gamma)\pi(1+\tau)}{d}}{\sinh\dfrac{\exp(\mathrm{i}\gamma)\pi(1-\tau)}{d}}}\left(\coth\left(\frac{\pi(\tau\exp(\mathrm{i}\gamma)-z)}{d}\right)-1\right)\exp(\mathrm{i}\gamma)\,\mathrm{d}\tau,\end{aligned} \tag{16}$$

where the prime notation means a differentation with respect to the chordwise coordinate x_1^*; $y_{c,v}$ and $y_{th,v}$ represent the camber and thickness distributions on the stator vane, and d the separation between two consecutive vanes in the infinite cascade. To scale the flow field, one should multiply v_x and v_y by the free stream velocity V and then add Vv_x and Vv_y to the axial and vertical free stream velocity components.

Eq. (16) is solved at each spanwise location R and the resulting flow field is calculated at a distance s from the cascade leading edge by superimposing the perturbations Vv_x and Vv_y to the undisturbed field represented by V_{iA} and V_{iT} obtained respectively by Eqs. (14) and (15). To consider the possibility of having an uneven azimuthal distribution of the vanes, such as in the UB/UV configuration, the following approach is used:

- For each couple of vanes v and $v+1$ spaced by $d = R\Delta\theta_v = R(\theta_{v+1} - \theta_v)$, the flow field of an infinite cascade of vanes with separation d at distance s from the cascade leading edge is computed.
- Only the flow field in the interstage between two consecutive vanes is extracted.

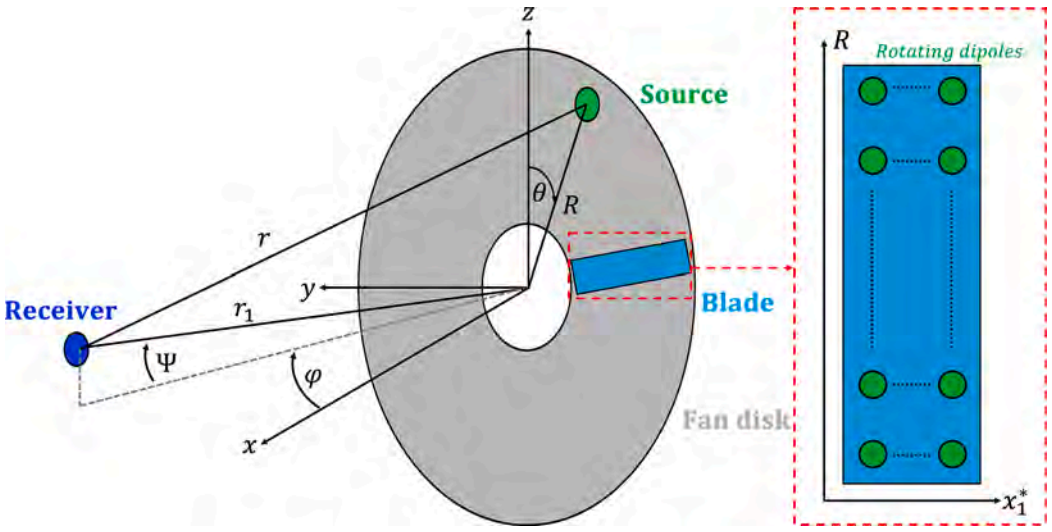


Fig. 7. Schematic view of the noise calculation and of the blade discretization.

- The procedure is repeated until all the vane couples are considered.
- The computed velocity flow fields are stitched consecutively ensuring a smoothing transition between the $V-1$ segments by means of a Tukey windowing function [49].

It should be noted that the reconstruction procedure adopted for unevenly spaced vanes does not consist of stitching together isolated airfoil solutions. For each pair of consecutive vanes, the disturbance field is computed using the infinite cascade formulation with the corresponding local inter-vane spacing. Therefore, each extracted flow-field sector already includes the cascade interaction effects associated with the corresponding periodic cascade configuration. The stitching procedure is used to reconstruct the full circumferential distribution of the forcing field from the locally periodic solutions. Although this approach remains an approximation, it enables the dominant cascade effects to be retained while accounting for uneven vane spacing at a negligible additional computational cost.

3.5. Far-field noise calculation

Each segment in both chordwise and spanwise directions is modeled as a compact dipole and the resulting noise at a probe located at $\vec{r}_1 = \{x, y, z\}$ in the far-field is calculated by means of the FW-H acoustic analogy in the frequency domain [6,50]. The model assumes that the blades are flat plates collapsed on the fan disk, following a planform approximation.

Following the reference frame sketched in Fig. 7, the Fourier coefficient of the acoustic pressure at the frequency $f = n\Omega$ produced by a rotating compact dipole located at a distance $\vec{r} = \{x, y - R\cos\theta, -R\sin\theta\}$ with respect to the far-field probe is calculated as

$$\begin{aligned} c_n = & \frac{in\Omega \exp\left(\frac{in\Omega r_1}{c_0}\right)}{4\pi r_1 c_0} \sum_{b=1}^{B} \sum_{i=1}^{N_s} \sum_{j=1}^{N_c} \sum_{k=-\infty}^{+\infty} \tilde{T}_{i,j,k,b} \cos\varphi J_{n-k}(nM\sin\varphi) \exp\left[-i(n-k)\Psi_b\right] + \\ & + \frac{\tilde{\Theta}_{i,j,k,b}\sin\varphi}{2i} \Big\{ J_{n-k-1}(nM\sin\varphi) \exp\left[-i(n-k-1)\Psi_b\right] + \\ & - J_{n-k+1}(nM\sin\varphi) \exp\left[-i(n-k+1)\Psi_b\right] \Big\}, \end{aligned} \tag{17}$$

where $J_\nu(x)$ is the νth order Bessel function of the first kind, $\Psi_b = \theta_b - \Psi + \pi/2$, and $\tilde{T}_{i,j,k,b}$ and $\tilde{\Theta}_{i,j,k,b}$ are respectively the axial and radial components of the blade loading harmonics of the ith spanwise and jth azimuthal (chordwise) segments, at a frequency $f = k\Omega$, for the bth blade obtained with Eq. (4). For low-speed axial fans, the radial component can be neglected [4]. The SPL in dB at $f = n\Omega$ is then obtained from Eq. (17) as

$$SPL_n = 20\log_{10}\left(\frac{2|c_n|}{2\cdot 10^{-5}}\right). \tag{18}$$

The factor 2 in Eq. (18) is required since the SPL spectrum is shown as single-sided while the blade loading harmonics are computed as double-sided.

4. LBM and RANS simulations setups

High-fidelity CFD simulations have been employed both for the validation of the analytical model and for the extraction of its input data. The engine cooling fan, shown in Fig. 1a, has been simulated in an open environment through a sufficiently large computational domain surrounding the fan, so as to reproduce free-field sound propagation conditions. A detailed comparison of integral quantities and flow features between LBM and RANS simulations is provided in Section 6.1.1.

4.1. LBM

First, scale-resolved simulations based on the LBM [51] have been performed using the commercial software 3DS PowerFLOW version 6. To reduce the computational cost, a Very Large Eddy Simulation (VLES) approach has been used, thus resolving only the largest turbulent scales. The subgrid model implemented in the software is derived from the renormalization group $k-\epsilon$ transport equations (RNG $k-\epsilon$) [52]. The wall model used by PowerFLOW is the pressure-gradient extended wall model (PGE-WM), which is an extension of the generalized wall model proposed by Launder and Spalding. For more details the reader is referred to [53,54].

The mesh resolution has been decreased when increasing the distance from the cooling module by following a Variable Resolution (VR) regions approach [55]. The finest VR region has been set as an offset of the rotor and including additionally the tip clearance, so that it could be ensured the presence of at least 10 cubic cells (voxels) in the tip clearance. The fluid domain has been discretized with a resolution of 1200 voxels per diameter in the finest VR region, leading to a grid of 360 million fine equivalent voxels. This resulted in a cut-off frequency of the direct numerical probe approximately equal to $f_{cut-off}/BPF = 8$. The independence of the solution from the mesh size has already been assessed in a previous study [38]. Approximately a rotation of 0.04° per timestep has been simulated for a period of 20 fan revolutions. Data has been recorded only on the last 10, resulting in a computational cost of approximately 58000 CPU hours. Further details on the computational setup used to perform the LBM simulations can be found in previous works [38,56], in which the simulations were validated against experimental results.

The acoustic field has been sampled directly from the simulations at each timestep on a fully circular array of 12 equally spaced far-field probes, located in the plane xy at a radius $r_1/D = 2.15$ upstream of the fan rotational axis. In addition, the instantaneous surface pressure distribution on the blades has been sampled with a frequency of 48 kHz. Thereafter, the unsteady pressure has been propagated to the same probe locations in the far-field by means of the solid formulation of FW-H analogy in PowerFLOW [57]. The spectral content of the acoustic signals has been computed through the Welch periodogram method [58] with 4 Hamming windows and 50% of overlap, resulting in a frequency resolution of 11 Hz. When comparing the SPL from LBM simulations against the analytical model results, a harmonical reconstruction has been obtained by integrating the SPL in a frequency band of width $\Delta f/\Omega = 1$, centered at frequencies multiple of Ω.

4.2. RANS

Wall-resolved incompressible steady RANS simulations have been performed using the Ansys CFX commercial software. To reduce the computational cost of the simulation, a single blade passage with periodic boundary conditions has been simulated. The corresponding azimuthal sector that has been simulated is equal to 32°.

The $k-\omega$ SST turbulence model has been adopted, and a second-order implicit scheme has been employed to discretize the governing equations in space. The coupled solver has been used.

An unstructured mesh to discretize the fluid domain has been utilized. Three different mesh resolutions have been simulated, to assess the independence of the solution from the grid. The coarse grid has 6.6 million elements, the medium grid 9 million elements, and the fine grid 26 million elements. The mesh refinement has been performed by increasing the element base size by a factor of 2.

Mass flow rate is imposed as inlet boundary condition, while static ambient pressure is imposed as outlet boundary condition. This amounts to a slight pressure difference between upstream and downstream.

To simulate the blade rotation, the frozen rotor approach has been utilized. The computational cost ranged approximately between 500 (coarse grid) and 2000 (fine grid) CPU hours.

5. Noise sources characterization through the LBM simulations

The noise sources for both the EB/EV and UB/UV configurations are assessed from the LBM simulations. This analysis is intended to verify whether the dominant tonal noise generation mechanisms are associated with flow features explicitly accounted for in the analytical model, and to identify additional source mechanisms that may be present in the simulations but are not included in the model. Fig. 8 shows the spectra of pressure fluctuations at $r_1/D = 2.15$ and $\varphi = 0°$ (on the fan rotational axis), as sketched in the lower right corner of the figure. The solid lines refer to the pressure signal directly sampled from the simulation, while the dashed lines refer to the pressure signal obtained by propagating only the blade surface pressure fluctuations with the solid formulation of the FW-H analogy. The direct probe and FW-H signals match within small differences that never exceed 3 dB/Hz, meaning that the noise sources of this fan system are dominated by rotor noise. Moreover, the EB/EV configuration is characterized predominantly by broadband noise, whereas the UB/UV configuration exhibits several narrowband peaks at the BPF, its harmonics, and subharmonics. The substantial increase in tonal levels observed for the UB/UV configuration is associated with the loss of circumferential symmetry introduced by the uneven blade and vane spacings. This redistributes the interaction energy into additional harmonic and subharmonic components, including acoustic modes capable of radiating efficiently on the fan rotational axis. This behavior is consistent with

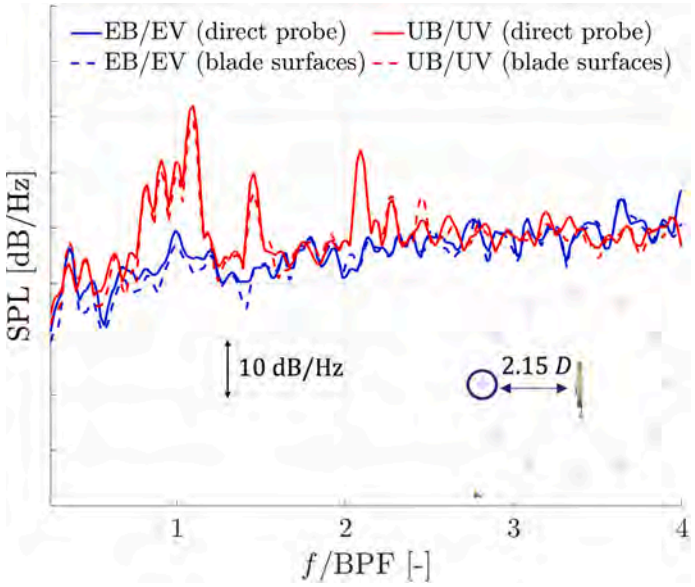


Fig. 8. Pressure fluctuations in dB/Hz from the LBM simulations at $r_1/D = 2.15$ and $\varphi = 0°$ (along the rotational axis).

previous studies [39,59], which showed that uneven blade and vane spacing tends to redistribute tonal energy from the BPF harmonics onto rotational ones. By contrast, the EB/EV configuration does not exhibit pronounced tonal peaks on the fan rotational axis. In this configuration, the dominant rotor-stator interaction generates circumferential acoustic modes associated with the vane harmonic order V. However, for an observer located on the rotational axis ($\varphi = 0°$), only axisymmetric acoustic modes can radiate, while contributions in the acoustic pressure related to non-axisymmetric modes vanish due to the Bessel function dependence of the acoustic field. As a result, the tonal rotor-stator interaction contribution becomes weak on the fan rotational axis and the spectrum is dominated by broadband rotor noise.

The spatial distribution of the unsteady pressure is analyzed by applying a narrow bandpass filter to the fan surface pressure signals, as shown in Fig. 9, on the pressure side, for both the EB/EV and UB/UV configurations. Only the pressure side is shown since no inflow distortions upstream were identified. The filtering operation is used here as a visualization tool to isolate the noise sources associated with selected interaction frequencies. The frequency bands are centered at $f/\Omega = B$ and $f/\Omega = V$. The bandwidth of the bandpass filter is $\Delta f/\Omega = 1$. The pressure is made dimensionless by the dynamic pressure at the tip $p^{\circ}_{tip} = 1/2\,\rho v^2_{tip}$. At the BPF and harmonics, the EB/EV configuration shows almost zero pressure amplitude up to a narrow spanwise region at the tip. On the contrary, the UB/UV configuration is characterized by local higher amplitude regions that are uniform in the spanwise direction and are azimuthally aligned with the stator vanes. This is the result of the rotor-stator non-viscous (i.e., potential) interaction which redistributes its energy among several frequencies due to the uneven spacing of blades and vanes. Moreover, at $f/\Omega = V$, the EB/EV configuration shows higher amplitude values on the whole blade span with respect to the UB/UV configuration as a result of concentrating all the energy at one fundamental frequency in the evenly spaced configuration. This component corresponds to the fundamental frequency at which an individual rotor blade encounters the V-periodic potential field generated by the evenly spaced stator vanes. Therefore, $V\Omega$ represents a characteristic rotor blade loading frequency of the rotor-stator potential interaction. The resulting acoustic field satisfies the rotor-stator circumferential mode selection rules and contains tonal frequencies at the BPF harmonics, while the vane count determines the associated azimuthal mode orders. Along the rotational axis, only the axisymmetric component contributes, which strongly restricts the rotor-stator interaction tones observable at this probe location. Finally, the pressure peaks at the tip, distributed along the whole blade chord and visible at all the analyzed frequencies, are the trace of vortical structures that are due to flow separation at the tip, on the blade pressure side. As a matter of fact, this behavior is characteristic of the free blowing operating condition [38,56].

Although the present analysis was performed for an open fan configuration, some qualitative considerations can be drawn regarding installation effects. The presence of upstream cooling module components, such as heat exchanger and casing, is not expected to modify the rotor-stator potential interaction mechanism itself, although changes in the mean flow field and blade loading will affect the resulting tonal amplitudes [60]. Conversely, ducted configurations introduce additional acoustic propagation and modal effects. In such cases, the radiated tonal content depends strongly on the cut-on behavior of the acoustic modes governed by the blade and vane counts according to the Tyler and Sofrin rule, potentially altering the relative importance of rotor-stator interaction tones. Moreover, changes in the tip clearance flow should also be considered, as stronger and more coherent vortex structures increase broadband noise and, in addition, generate tonal components that can compete with rotor-stator interaction tones [61].

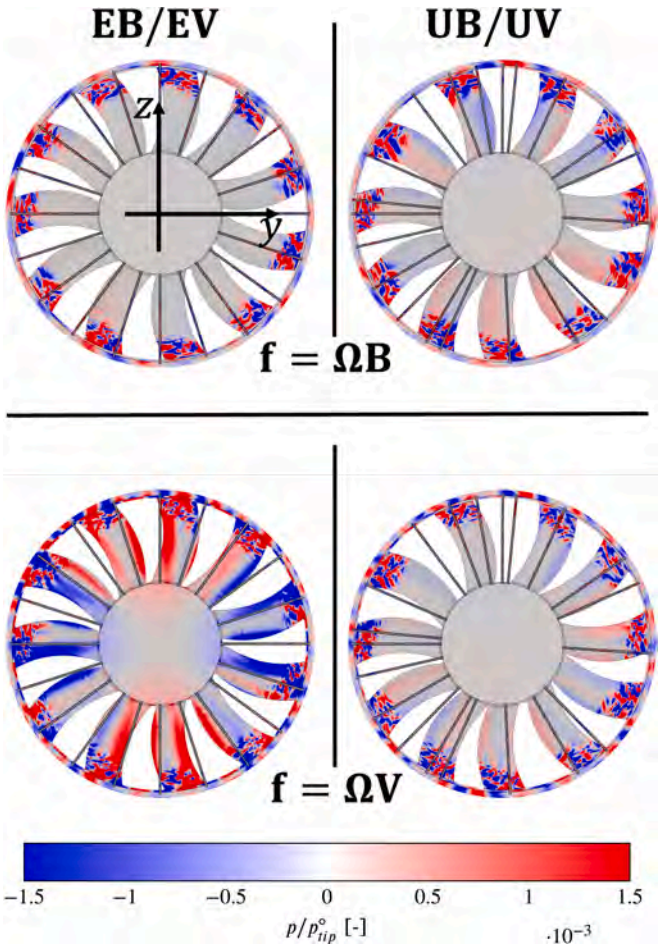


Fig. 9. Bandpass filtered surface pressure on the fan (view of the blade pressure side). The vanes surface is left only as a visual reference.

Table 1
Summary of the computational cost of each simulation approach.

	LBM	RANS	Model
CPU Hours	58k	2k	0.025-0.25
Speed-up wrt LBM	1x	29x	2320x - 232x
Speed-up wrt RANS	0.035x	1x	1160x - 116x

6. Results and discussion

Each blade is discretized with $N_s = 10$ points in the spanwise direction and $N_c = 20$ points in the chordwise direction following the convergence study described in Appendix C. In the remainder of this section aerodynamic and acoustic comparisons between the analytical model and the reference LBM simulations are presented. The analytical model is fed with different input flow fields:

- Time-averaged flow field obtained from the reference LBM simulations. It is used for validation purposes only.
- Steady flow field obtained from the RANS simulations. This represents a possible trade-off input to the model.
- Gaussian velocity deficit rescaled with the potential flow field past a Joukowski airfoil.
- Potential flow field past an airfoil cascade including the actual airfoil shape.

Table 1 shows a summary of the computational cost of each simulation approach (LBM, RANS, analytical model) with the relative speed-up with respect to both the LBM and the RANS simulations.

Table 2
Grid independence study for the RANS simulations. Thrust and torque have been made dimensionless with the corresponding time-averaged LBM values.

	T_{RANS}/T_{LBM} [-]	Q_{RANS}/Q_{LBM} [-]
Coarse	0.9560	0.9468
Medium	0.9674	0.9495
Fine	0.9666	0.9506
Inf	0.9667	0.9509

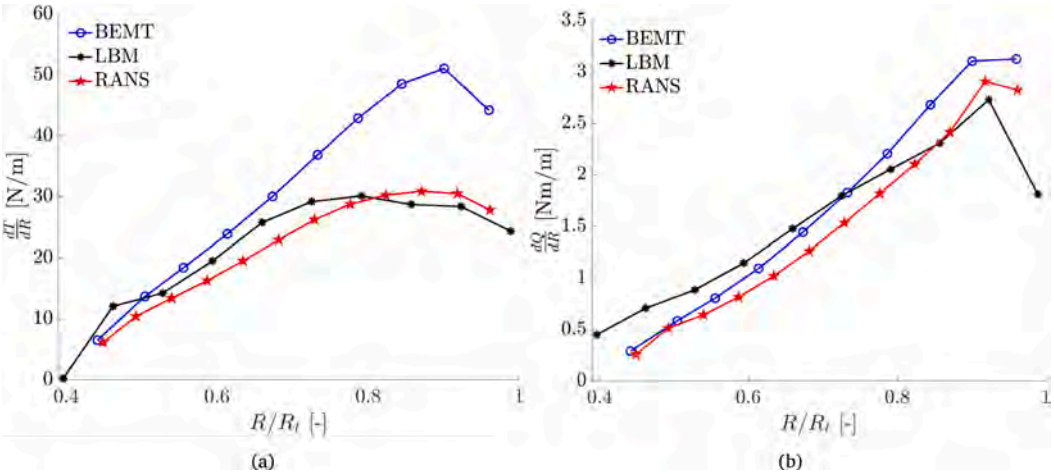


Fig. 10. Sectional spanwise distribution of thrust and torque derivatives on one blade sampled from the LBM, the RANS, and computed with the BEMT model. (a): Thrust. (b): Torque.

6.1. Aerodynamic results

6.1.1. Steady loading calculation

Table 2 shows the thrust and torque on the blades in terms of the ratio between the RANS and time-averaged LBM simulations over the last 10 revolutions for the three mesh sizes of the RANS simulations. The "Inf" values are obtained through a Richardson extrapolation [62] with a refinement ratio $r = 2$ and order of convergence $p = 2$ [55]. Both the thrust and torque are slightly underestimated by the RANS although by maximum 5%. However, the mesh independence is considered to be reached on the fine mesh, as the thrust and torque both approach the asymptotic values obtained with the Richardson extrapolation. Thus, the remainder of this paper will consider only the fine grid for the RANS simulations as input flow field for the analytical model.

Fig. 10 shows the sectional spanwise distribution of the thrust (Fig. 10a) and torque (Fig. 10b) derivatives on one of the 11 identical blades, both sampled from the LBM, the RANS, and computed with the BEMT model outlined in Section 3. It should again be noted that the LBM simulations are employed in the present work as a high-fidelity aeroacoustic reference rather than as a replacement for RANS approaches in the prediction of global aerodynamic quantities. While RANS methodologies are widely adopted and sufficiently accurate for mean flow and integral force predictions, the present study also requires the resolution of unsteady tonal fluctuations and direct acoustic propagation. In this context, the LBM framework provides a consistent aeroacoustic reference by simultaneously resolving the flow and acoustic fields within the same compressible simulation framework. Moreover, the present LBM simulations represent the closest approximation to an experiment that was available.

Fig. 10 shows that, for $0.55 \leq R/R_t \leq 0.8$, both the thrust and torque derivatives are underestimated by the RANS and BEMT with respect to the LBM, although the shape is preserved. The BEMT underestimation is attributed to the lack of any information about the loading increase given by the presence of stator vanes, which is expected to influence the angle of attack. Moreover, the BEMT approach does not consider solidity effects, which are expected to play a role in fans such as the one analyzed in this work. Finally, the c_l and c_d predictions obtained with XFOIL might not be accurate due to the off design operating condition in which the fan is simulated and a proper tuning of N_{crit} value should be done along the spanwise sections. The RANS underestimation is attributed to the slight differences in the numerical setup with respect to the LBM one as discussed in Section 4.2. Moreover, the RANS simulations assume a perfect axisymmetry of the whole rotor-stator assembly, which does not hold due to the shape of the shroud and the fact that the number of blades (11) and vanes (20) are coprime numbers. Nevertheless, the differences between LBM, RANS, and BEMT are under 10% when computing the integral thrust and torque values. Thus, the approach is considered sufficiently accurate for the purposes of the remaining modeling workflow.

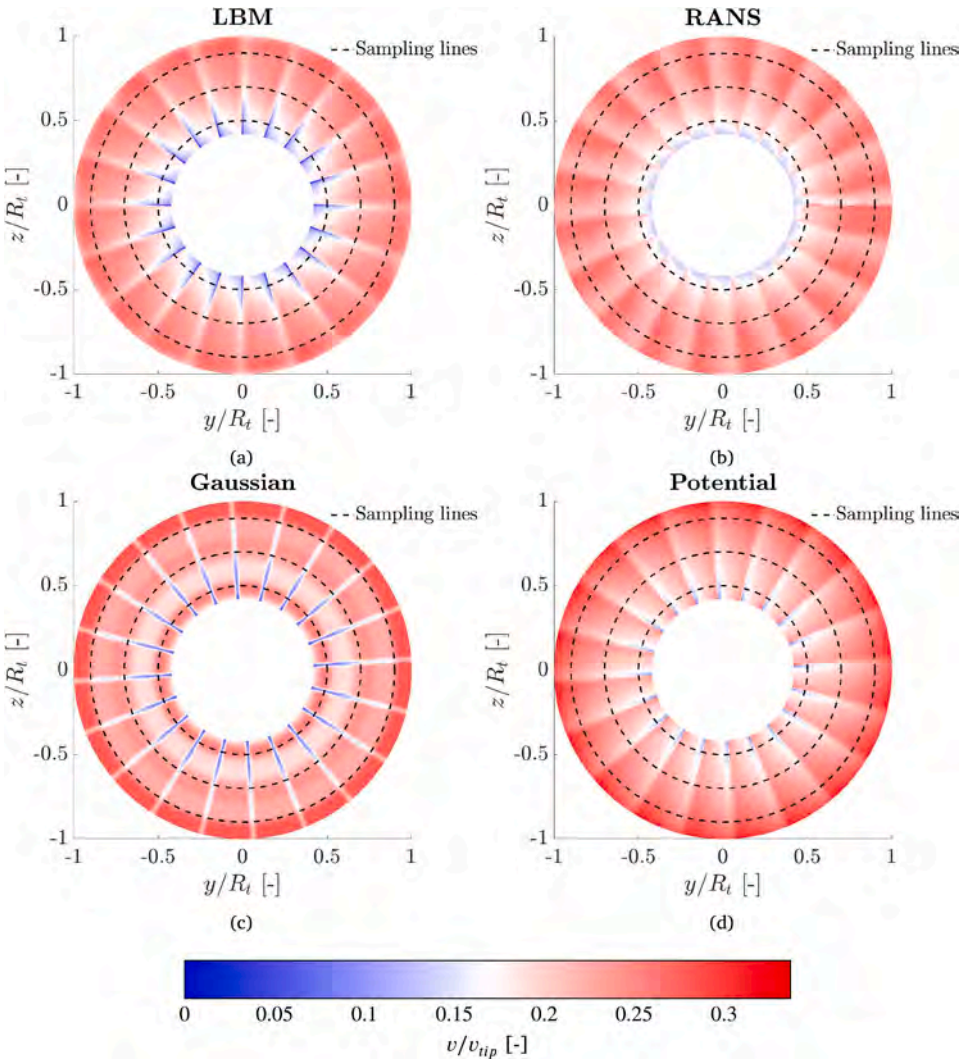


Fig. 11. Time-averaged upwash velocity contours $0.0075D$ downstream of the blade trailing edge for the EB/EV configuration. The quantity has been made dimensionless with the tip velocity $v_{tip} = \Omega R_t$. (a): LBM. (b): RANS. (c): Gaussian. (d): Potential.

6.1.2. Flow field at the blades trailing edge

Figs. 11 and 12 show the contours of the dimensionless time-averaged upwash velocity for both EB/EV (Fig. 11) and UB/UV (Fig. 12) configurations sampled $0.0075D$ downstream of the blade trailing edge. Results from LBM and RANS simulations as well as the ones obtained with the two analytical approaches proposed in Section 3 are shown. The "Gaussian" label refers to the approach based on the assumption of a Gaussian velocity deficit at the stator vanes location, while the "Potential" label refers to the approach based on the airfoil cascade equations.

Both EB/EV and UB/UV configurations are similar in terms of spanwise velocity distribution; the only tangible difference is the azimuthal location of the velocity deficit induced by the vanes. The RANS flow field is similar to the LBM one, especially in terms of radial distribution of the velocity, thus giving confidence that the reconstruction of the full flow field can be performed from the RANS single blade passage even in the presence of an uneven distribution of stator vanes. However, the RANS flow field shows a slightly higher diffusion that is attributed to the differences in the numerical setup as well as to the intrinsic higher numerical diffusivity of the NS approach with respect to the LBM one. Both the Gaussian and Potential flow fields show trends of the velocity radial distribution qualitatively similar to the LBM. The Gaussian flow field, however, is characterized by a thicker velocity drop with respect to the LBM, indicating that the velocity drop shape is not correctly computed with this approach. On the contrary, the Potential flow field shows a more similar behavior with respect to the LBM although minor differences are spotted.

To quantitatively assess the differences between these flow fields, the upwash velocity $0.0075D$ downstream of the blade trailing edge is extracted at several spanwise positions R along circular lines as sketched in Figs. 11 and 12. Fig. 13 shows the azimuthal profile of the upwash velocity for both EB/EV (Fig. 13a) and UB/UV (Fig. 13b) configurations, on a quarter of circumference. Both the RANS-

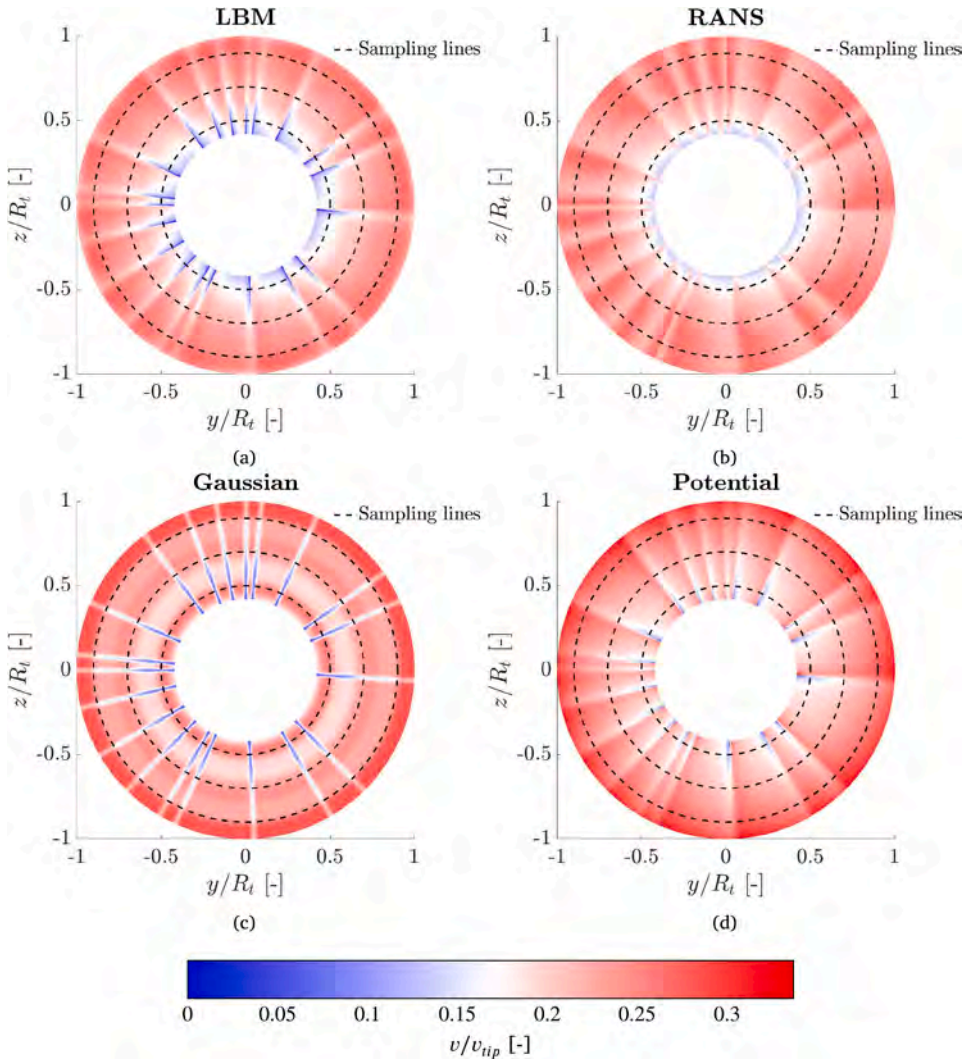


Fig. 12. Time-averaged upwash velocity contours $0.0075D$ downstream of the blade trailing edge for the UB/UV configuration. (a): LBM. (b): RANS. (c): Gaussian. (d): Potential.

based and fully analytical flow field reconstructions predict the velocity drops in correspondance of the stator vane azimuthal locations for both EB/EV and UB/UV configurations. The RANS solution shows lower amplitude with respect to the LBM one, attributed to the slightly higher numerical diffusivity. However, this happens only for $R/R_t = 0.50$, thus suggesting that it does not affect much the far-field acoustics. The Gaussian model shows a flat velocity profile outside of the vanes region of influence, which does not correspond to what seen in the LBM flow field. This suggests that the assumption of a Gaussian velocity deficit at the vane locations is not physically correct, as the azimuthal profile should show an increase and decrease when going from one vane position to the next one such as the Potential model green curve in Fig. 13. Moreover, the Gaussian profiles show an overestimation of the fluctuations amplitude, especially at midspan locations. The most accurate yet computationally efficient strategy to predict the time-averaged flow field in the rotor-stator interstage is the one based on the airfoil cascade. As a matter of fact, the model can almost correctly predict both the azimuthal shape and the fluctuations amplitude at every spanwise location.

Figs. 14 and 15 report the magnitude of the upwash velocity azimuthal Fourier transform $\tilde{v}$ at different spanwise locations for both configurations. The frequency location of the peaks is similar for all the approaches and for both the EB/EV and UB/UV configurations. The RANS-based flow field reconstruction leads, as expected, to a slightly lower amplitude of $\tilde{v}$ due to numerical diffusion, while the Gaussian approach shows an amplitude overestimation, particularly evident for $R/R_t \leq 0.6$. The Potential approach, instead, confirms the model capability to predict $\tilde{v}$, which is an essential input for the unsteady aerodynamic model.

6.1.3. Blade loading fluctuations calculation

The output of Eq. (4), fed with the different input flow fields shown in Figs. 14 and 15, is compared against the blade loading harmonics computed directly from the unsteady LBM simulations. In Figs. 16 and 17, the spanwise distribution of the chordwise

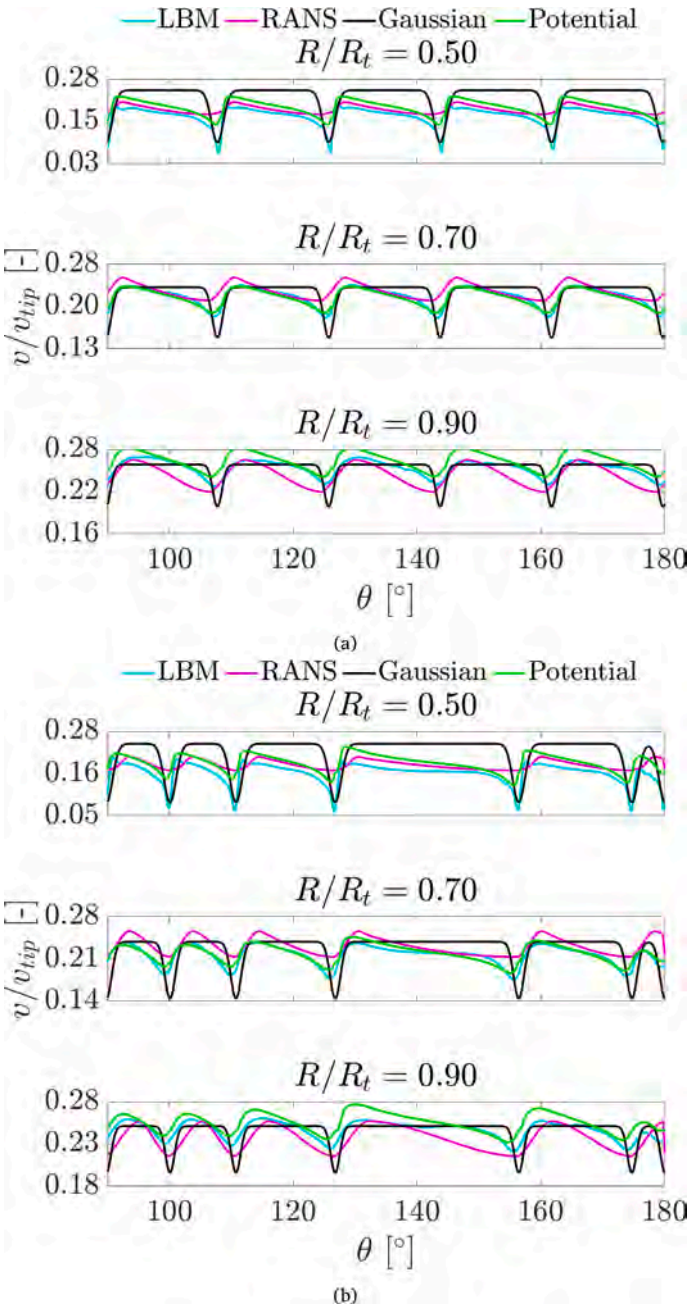


Fig. 13. Time-averaged upwash velocity azimuthal profiles $0.0075D$ downstream of the blade trailing edge. (a): EB/EV. (b): UB/UV.

integrated blade loading harmonics, $\tilde{F}$, is shown in the frequency range $w/B \in [-4, 4]$ for both the EB/EV (Fig. 16) and UB/UV (Fig. 17) configurations. The blade loading harmonics computed directly from the unsteady LBM simulations are named "Unsteady LBM", while the different input flow fields are named consistently with the previous plots (Figs. 11–15). The values of $\tilde{F}(w, x_1^*, R)$ have been integrated in $x_1^* \in [-1, 1]$. Similarly to what seen in Figs. 14 and 15, the model correctly calculates the frequency location of the peaks, especially in the EB/EV configuration, where the energy is concentrated at $w = \pm V$ and harmonics as a consequence of the rotor-stator potential interaction. Instead, the UB/UV configuration is characterized by a more broadband frequency content, as a result of the uneven spacing of both blades and vanes. The model correctly computes the blade loading amplitude up to $R/R_t = 0.7$, while for $R/R_t > 0.7$ it underestimates the amplitude due to the lack of any flow model that describes the unsteady flow features at the tip. However, the model does not well predict the low-frequency peaks seen in the unsteady LBM spectrum. These peaks are due to the blade interaction with the velocity deficit upstream caused by the four cuts on the shroud seen in Fig. 1a. Since this interaction

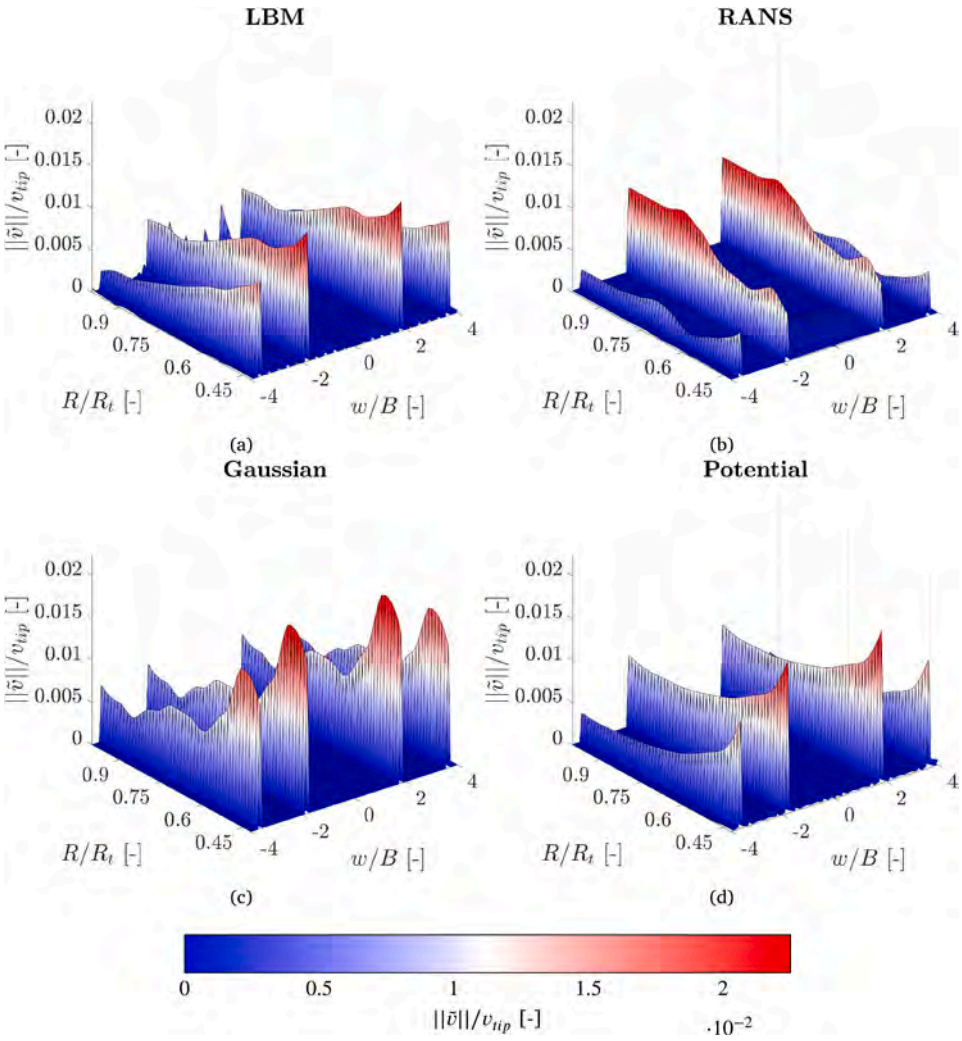


Fig. 14. Time-averaged upwash velocity azimuthal Fourier transform $0.0075D$ downstream of the blade trailing edge for the EB/EV configuration. (a): LBM. (b): RANS. (c): Gaussian. (d): Potential.

takes place only in a narrow annular region upstream, its contribution is less prominent in $\tilde{v}$.

Figs. 18 and 19 show the chordwise distribution of the blade loading harmonics in the frequency range $w/B \in [-4, 4]$ for both the EB/EV (Fig. 18) and UB/UV (Fig. 19) configurations. The values of $\tilde{F}(w, x_1^*, R)$ have been integrated in $R \in [R_h, R_t]$. As for the spanwise distribution in Figs. 16 and 17, similar conclusions can be drawn for the chordwise distribution. The frequency location of the peaks is correctly predicted by the model, as well as the more broadband content for the UB/UV configuration.

The validity range of the low-frequency approximation is assessed by computing the parameter

$$\mu = \frac{M}{1 - M^2} \frac{2\pi f c/2}{\Omega R}. \tag{19}$$

As reported by Amiet [63], the low-frequency approximation is valid for $\mu \leq \pi/4$. Fig. 20 reports the different values of μ at each spanwise station R. The low-frequency approximation is valid up to $f/BPF = 3$ at the hub and up to $f/BPF = 2.3$ at the tip. Hence, acoustic results for frequencies approximately higher than $f/BPF = 2.65$ might be less in accordance with the LBM simulations.

6.2. Acoustic results

In Fig. 21 the pressure fluctuations in the far-field at $r_1/D = 2.15$ and $\varphi = 0°$ (along the rotational axis) for the EB/EV and UB/UV configurations are shown. The red bar represents the signal directly sampled from the LBM simulations. The remaining bars represent the analytical model fed with the flow field sampled from the time-averaged LBM (light blue), RANS (magenta), and computed with the "Gaussian"" (black) and "Potential" (green) approaches. Results are shown at the BPF ($f/\Omega = B$), its first two harmonics ($f/\Omega = 2B$, $f/\Omega = 3B$), $f\Omega = V$ and its harmonic as well as the OASPL. The EB/EV configuration shows that the relevant tones are

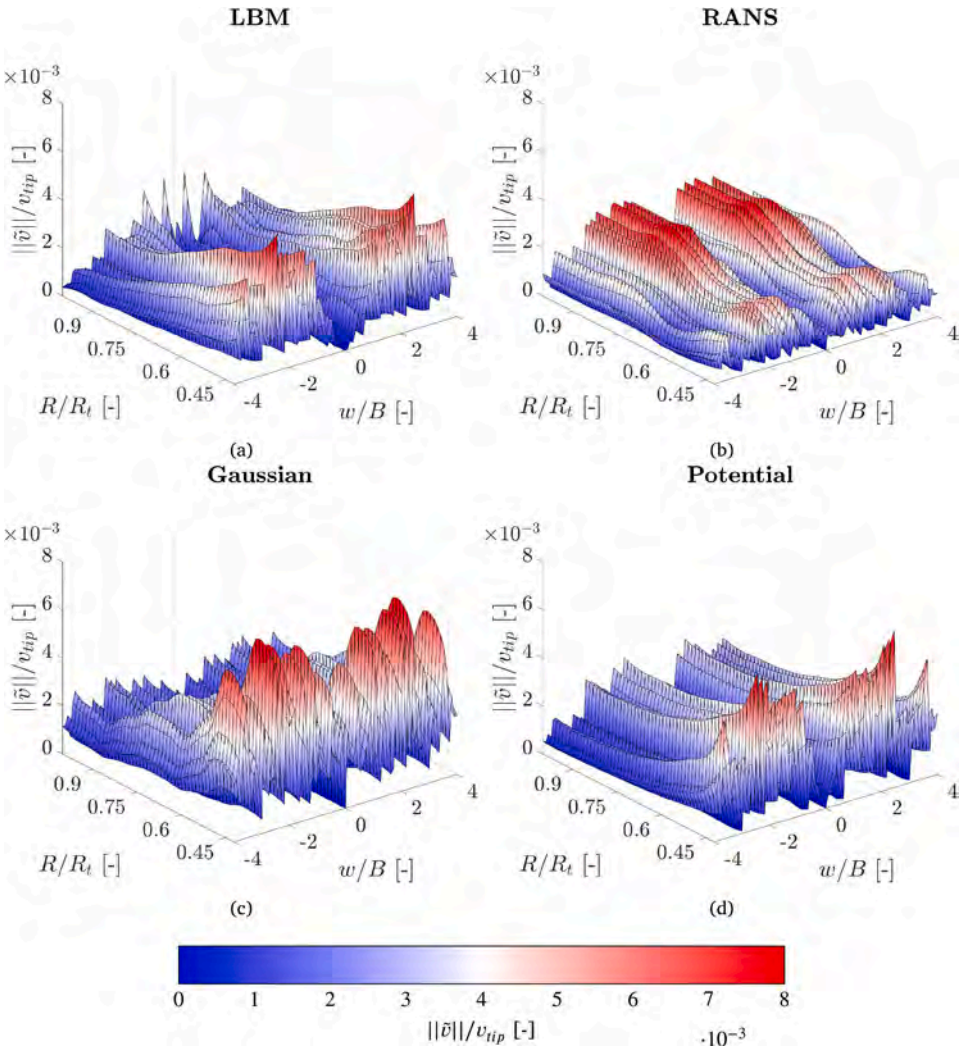


Fig. 15. Time-averaged upwash velocity azimuthal Fourier transform $0.0075D$ downstream of the blade trailing edge for the UB/UV configuration. (a): LBM. (b): RANS. (c): Gaussian. (d): Potential.

correctly predicted by the analytical model with respect to the reference LBM signals. Results obtained with the LBM and RANS input flow fields match the reference signals within 5 dB at $f/\Omega = B$ and $f/\Omega = V$. This is in line with the results obtained by Caro [64] and proves that a coupled RANS-Sears approach can also predict rotor-stator potential interaction noise, further relieving the necessity of using Unsteady RANS simulations to predict deterministic blade loading fluctuations [65]. Therefore RANS simulations can be used not only to predict broadband noise [66] but also unsteady deterministic tonal loading noise. Results obtained with the Gaussian and Potential input flow field tend to underestimate the tones. The lack of a broadband noise prediction in the analytical model prevents the correct calculation of noise levels at frequencies where deterministic rotor-stator interaction noise does not dominate ($f/\Omega = 3B$, $f/\Omega = 4B$). The UB/UV configuration shows instead a better match between the analytical model and the LBM simulations since the analytical model can correctly predict the tonal noise levels up to $f/\Omega = 2B$. At higher frequencies, the broadband contribution from the tip flow separation starts to outweigh the rotor-stator potential interaction tonal noise. Moreover, the breaking of the low-frequency approximation shown in Fig. 20 is responsible for the higher mismatch seen in the results for $f/\Omega > 2B$. The results shown in this paragraph highlight the feasibility of the presented approach also for custom blade and vane uneven spacing. Moreover, the computational advantage of the potential flow approach is stressed as well as its ease of implementation, which prevents the rise of both modeling and numerical issues as present in other low-fidelity approaches [67].

The analytical model capability to predict the variations in SPL between the UB/UV and EB/EV configurations at discrete frequencies is assessed. Fig. 22 shows the ΔSPL between UB/UV and EB/EV configurations for a far-field probe located at $r_1/D = 2.15$ and $\varphi = 0°$ (along the rotational axis). It can be observed that the analytical model can consistently predict the ΔSPL trend up to $f\Omega = 2B$. Consistently with the upwash velocity prediction, the Potential flow field provides a higher accuracy than the Gaussian one, closer to the time-averaged LBM and RANS flow fields. Moreover, it is seen that the direct probe and FW-H signals sampled from

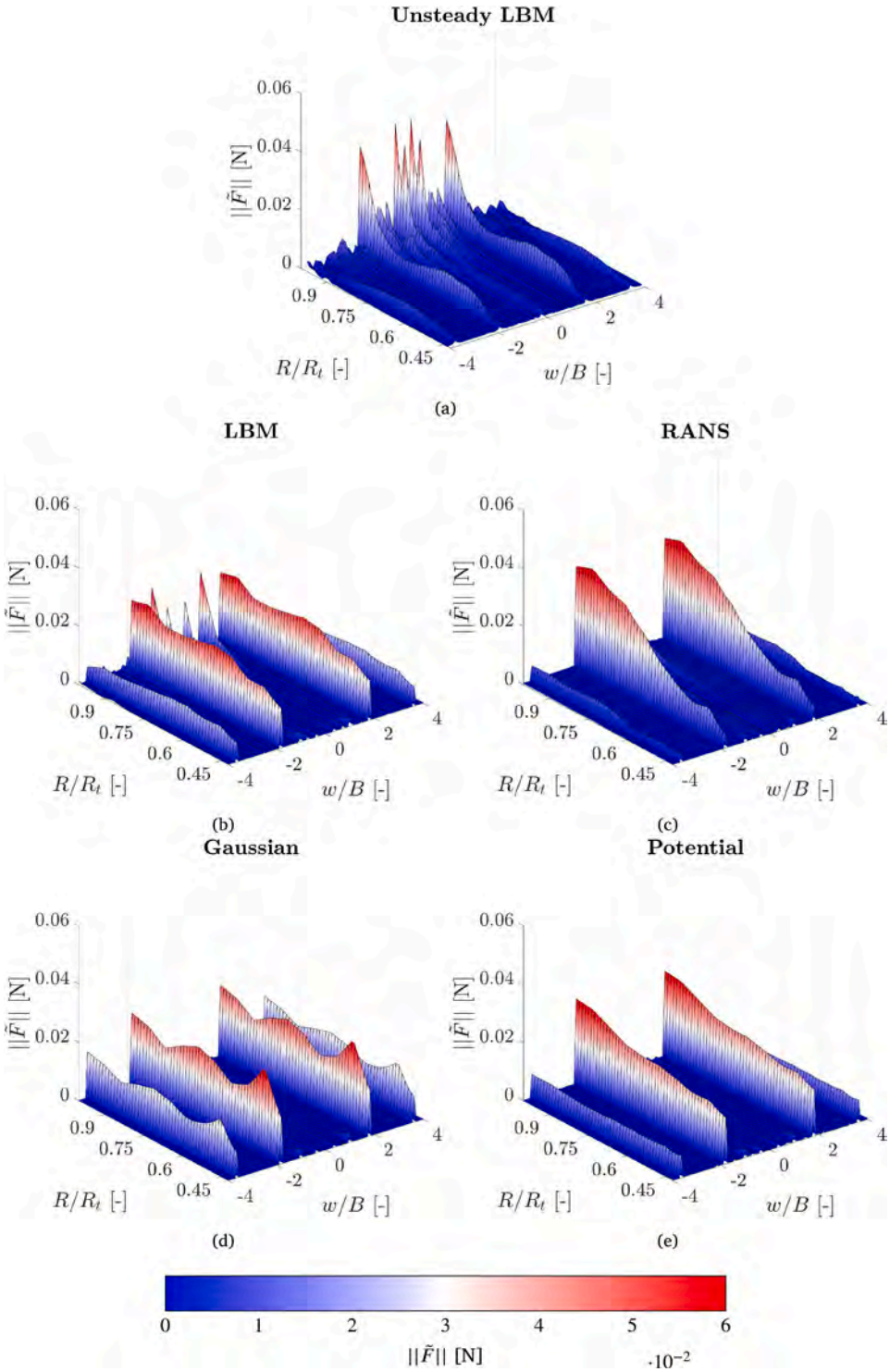


Fig. 16. Blade loading harmonics spanwise distribution integrated in the chordwise direction for the EB/EV configuration. (a): Unsteady LBM. (b): LBM. (c): RANS. (d): Gaussian. (e): Potential.

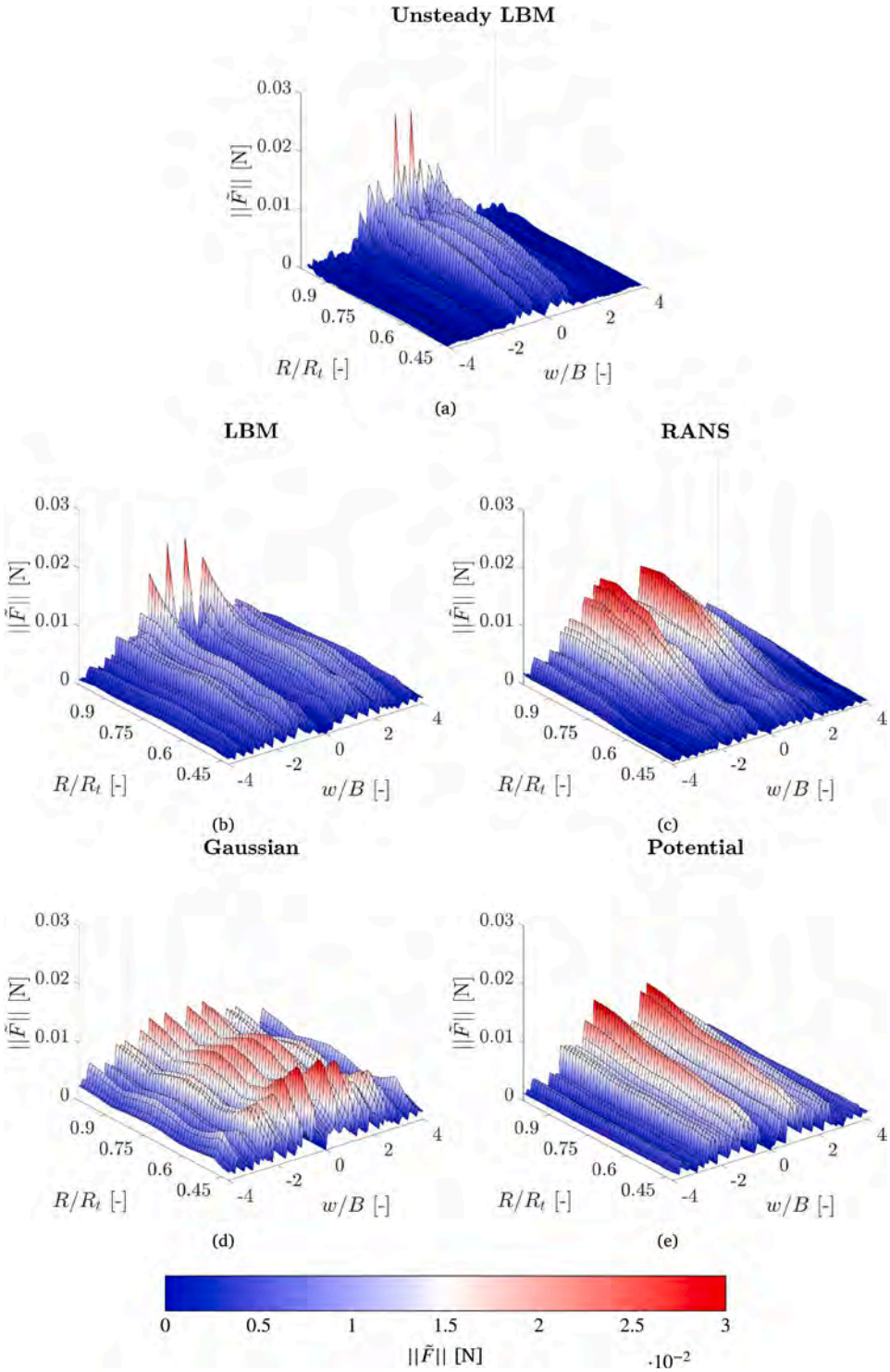


Fig. 17. Blade loading harmonics spanwise distribution integrated in the chordwise direction for the UB/UV configuration. (a): Unsteady LBM. (b): LBM. (c): RANS. (d): Gaussian. (e): Potential.

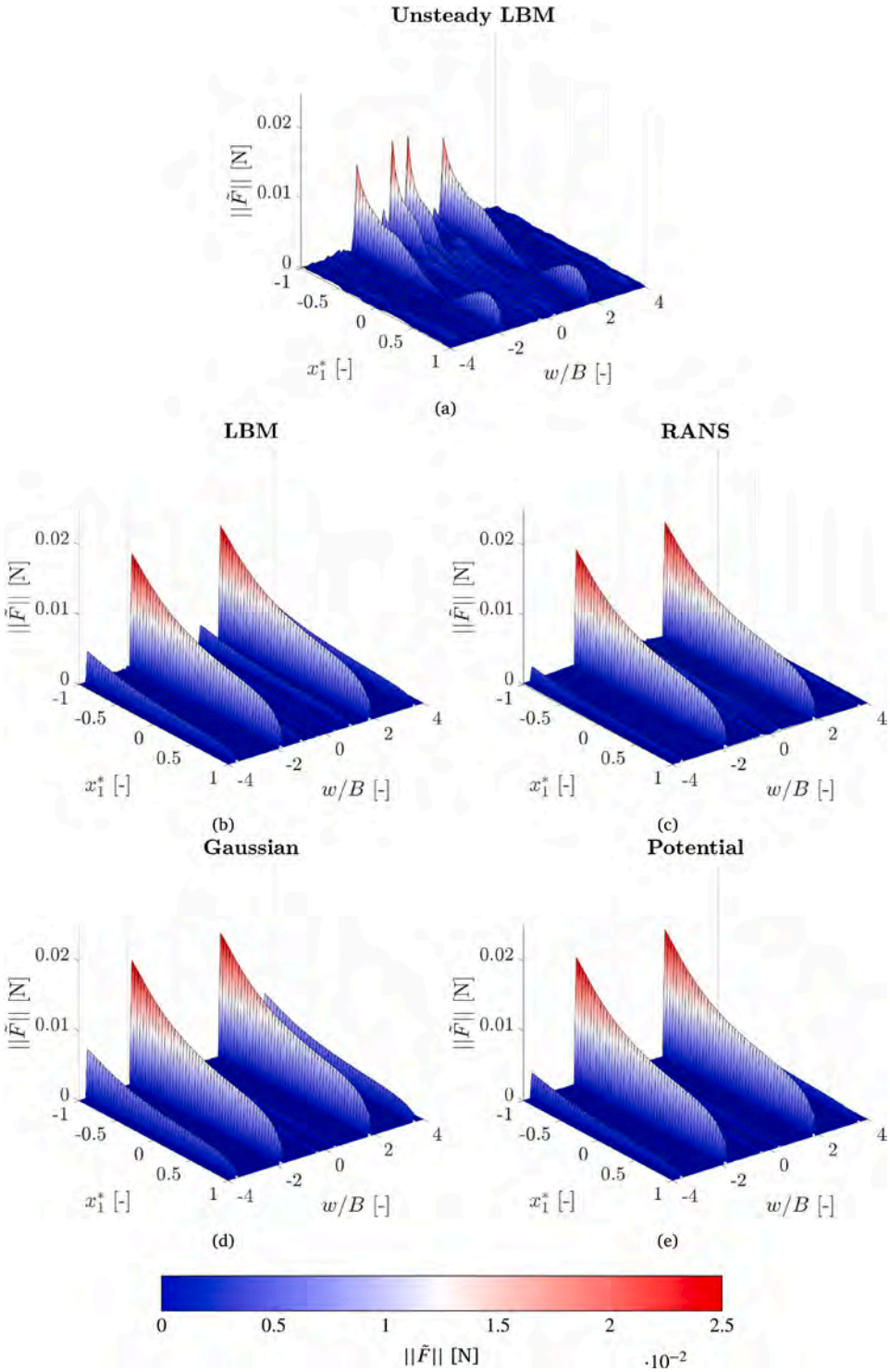


Fig. 18. Blade loading harmonics chordwise distribution integrated in the spanwise direction for the EB/EV configuration. (a): Unsteady LBM. (b): LBM. (c): RANS. (d): Gaussian. (e): Potential.

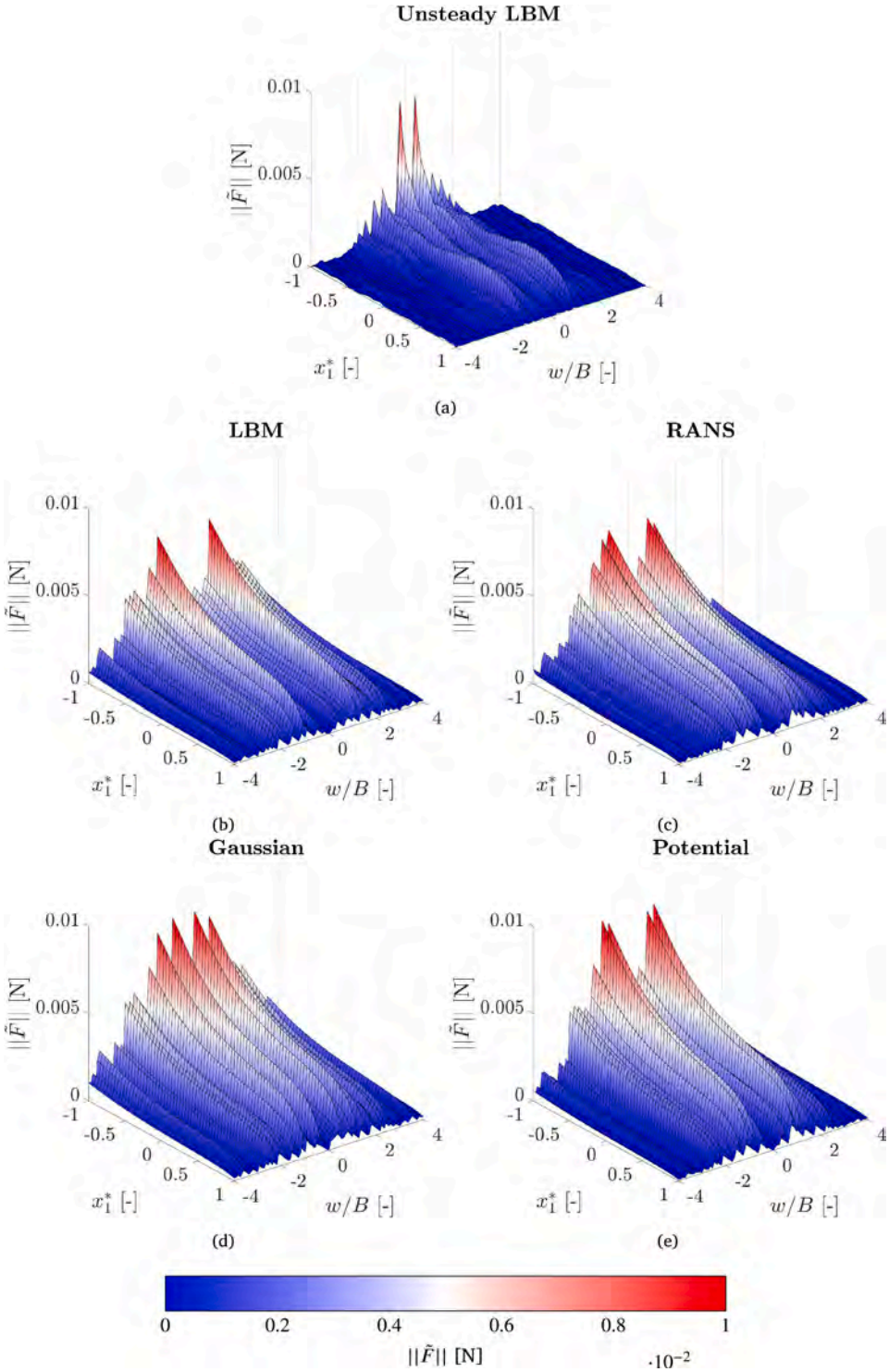


Fig. 19. Blade loading harmonics chordwise distribution integrated in the spanwise direction for the UB/UV configuration. (a): Unsteady LBM. (b): LBM. (c): RANS. (d): Gaussian. (e): Potential.

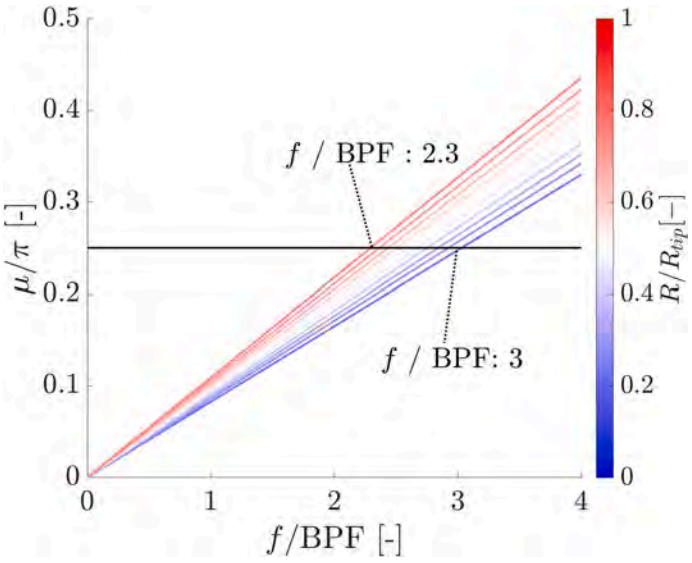


Fig. 20. Validity range of the low-frequency approximation.

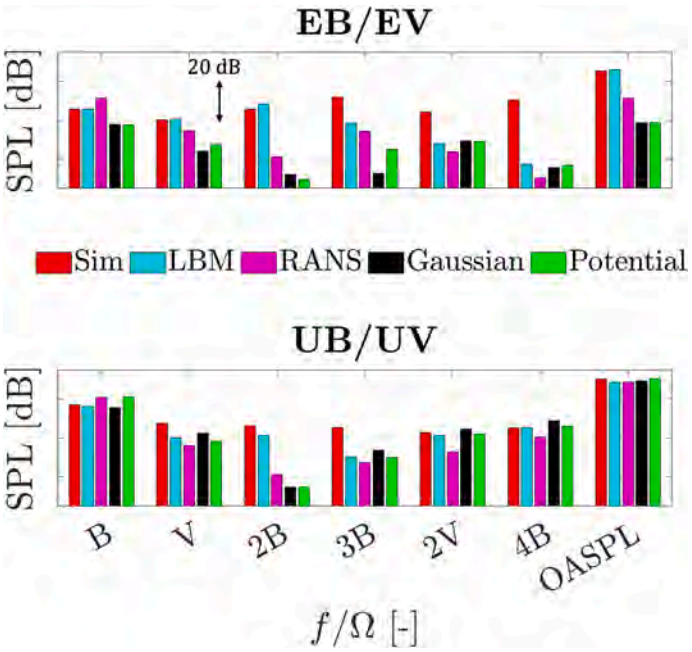


Fig. 21. SPL of far-field acoustic pressure in dB at $r_1/D = 2.15$ and $\varphi = 0°$ (along the rotational axis).

the LBM simulations slightly differ at higher BPF harmonics. At $f/\Omega = B$, the time-averaged LBM and RANS input flow field result in very similar ΔSPL values with respect to the reference signals. The RANS flow field slightly underestimates the ΔSPL, while the LBM flow field almost matches the reference ones. The Gaussian and Potential input flow fields result in higher ΔSPL with respect to the reference ones. At $f/\Omega = V$, all the input flow fields match well with the LBM signals except for the Gaussian one, which tends to overestimate the ΔSPL. This suggests that the main noise generation mechanism, i.e., the rotor-stator potential interaction, is accurately modeled, provided a sufficiently accurate time-averaged flow field as input. At $f/\Omega = 2B$, all the input flow fields are very close to the reference signals except for the LBM one, which underestimates the ΔSPL by 7 dB. Instead, at $f/\Omega = 3B$ there is a substantial overestimate of the ΔSPL for the Gaussian and Potential flow field inputs. The ΔOASPL is overestimated by the analytical model except for the LBM flow field input since the OASPL is underestimated for the EB/EV configuration, while correctly predicted for the UB/UV configuration, as seen in Fig. 21. Even though there is an evident discrepancy between the ΔSPL predicted by the analytical model and computed with the reference simulations, it should be noted that the frequency trend is retrieved with great

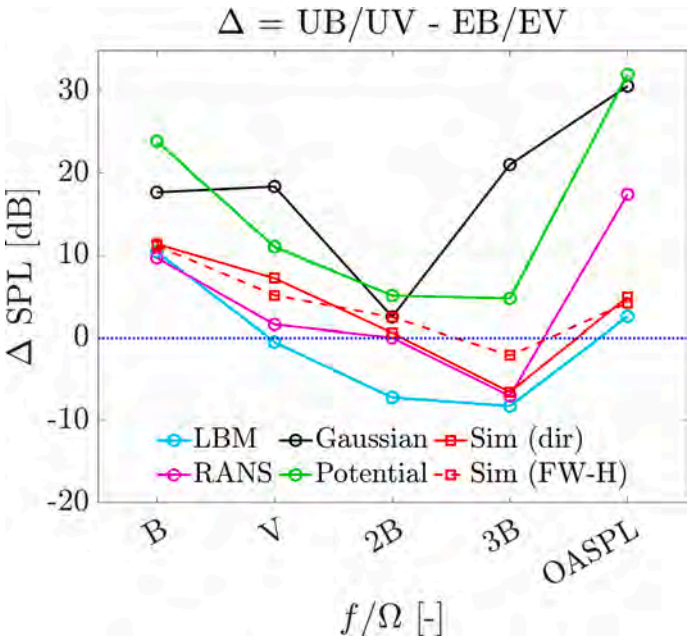


Fig. 22. SPL difference between the UB/UV and EB/EV configurations for a far-field probe located at $r_1/D = 2.15$ and $\varphi = 0°$ (along the rotational axis).

accuracy when using the LBM and RANS input flow fields and with sufficient accuracy when using the Potential input flow field; the Gaussian input flow field provides rather insufficient accuracy in the ΔSPL predicions due to the poorer reconstruction of the upwash velocity field. The analysis above confirms that a sufficiently accurate reconstruction of the time-averaged upwash velocity flow field leads to ΔSPL predictions that can be used for optimization purposes.

Finally, Fig. 23 shows the directivity patterns in the xy plane at $f/\Omega = B$, $f/\Omega = V$, $f/\Omega = 2B$, and for the OASPL in the frequency range $0 \leq f/BPF \leq 4$ for both the EB/EV (Fig. 23a) and UB/UV (Fig. 23b) configurations. It can be noted that there are differences between the LBM direct probe and the FW-H propagation of the blades surface pressure at $\varphi = 90°$ and $\varphi = 270°$. The EB/EV configuration (Fig. 23a) is characterized by a classical dipolar directivity at $f/\Omega = B$ and $f/\Omega = V$ that is correctly predicted by the analytical model and is in line with the FW-H propagation of the blades surface pressure. This means that sound scattering by other surfaces of the cooling module is present and dominates at microphone locations perpendicular to the fan rotating axis. At $f/\Omega = 2B$, the analytical model cannot predict well the directivity pattern computed with the LBM and highly underestimates noise levels. The underestimation at $f/\Omega = 2B$ as well as the lack of broadband prediction lead to systematic underprediction in the OASPL levels. However, the directivity pattern is correctly predicted. The UB/UV configuration (Fig. 23b) shows also that the analytical model predicts well the directivity pattern at both $f/\Omega = B$ and $f/\Omega = V$, while it underestimates the noise levels at $f/\Omega = 2B$ although by a smaller amount; it also correctly computes the directivity shape. Moreover, the OASPL levels are well predicted in this configuration as the rotor-stator potential interaction potential noise dominates over the broadband noise up to the first BPF harmonic, as shown in Fig. 8.

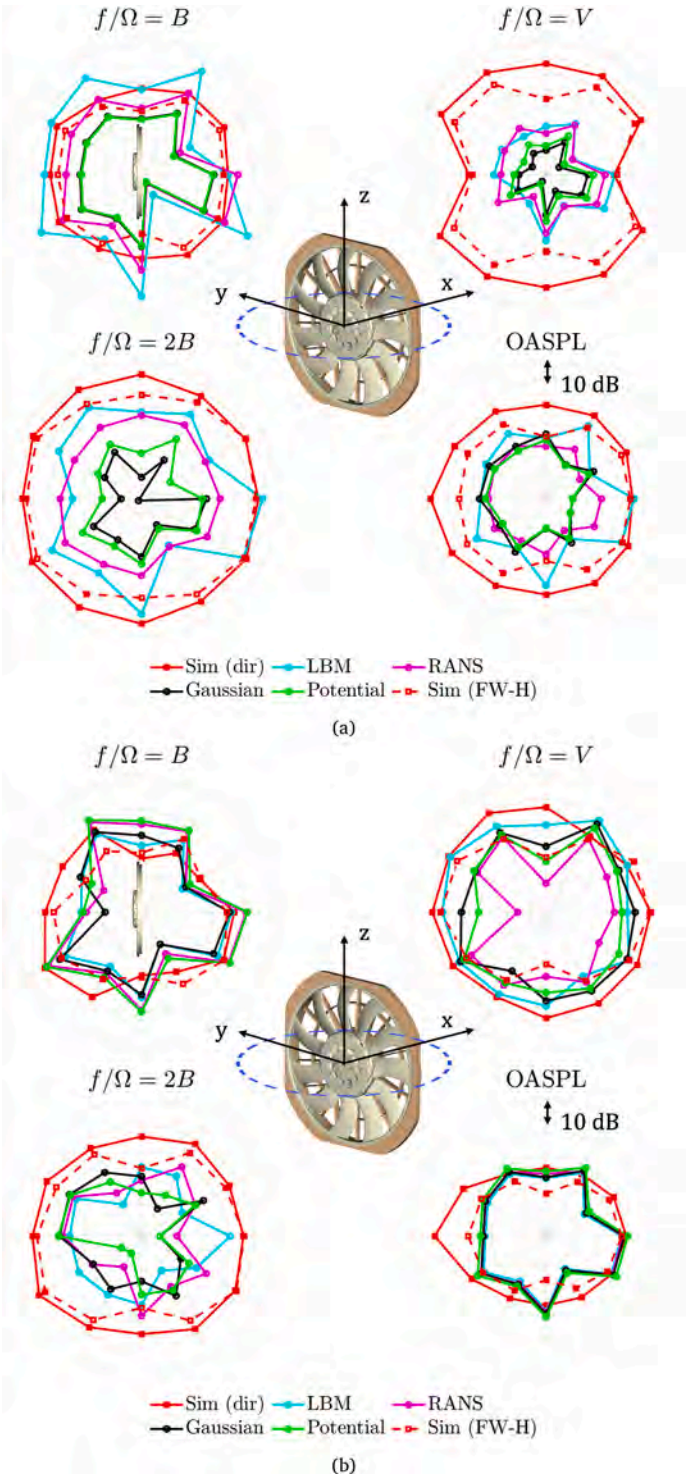


Fig. 23. Directivity plots in the xy plane of the far-field acoustic pressure in dB at $f/\Omega = B$, $f/\Omega = V$, $f/\Omega = 2B$, and the OASPL over the frequency range $0 \leq f/BPF \leq 4$. (a): EB/EV. (b): UB/UV.

7. Conclusions

This paper presents an analytical framework to predict rotor-stator interaction tonal noise in a low-speed axial cooling fan. Validation has been carried out against high-fidelity lattice-Boltzmann (LBM) simulations on two fan configurations with different blade and vane azimuthal distributions.

The analytical model propagates the blade loading in the far-field using the solid formulation of the FW-H acoustic analogy in the frequency domain. The BEMT is used to predict the steady blade loading while an unsteady aerodynamic formulation based on Sears' model is used to predict the unsteady blade loading. A key contribution is the modification of the pressure chordwise distribution function to reproduce the fluctuating pressure distribution of an airfoil rather than of a flat plate. A second novel contribution is the analytical reconstruction of the complete time-averaged velocity field based on potential-flow theory at the blade trailing edge. Two approaches have been assessed for this purpose: one relying on the assumption of Gaussian velocity deficit rescaled with the isolated airfoil potential flow solution, and the other employing a potential flow cascade-based solution on the stator vanes. Time-averaged flow fields from LBM and RANS with periodic boundary conditions are used as input to validate these approaches.

The BEMT solution is found to underestimate both the sectional thrust and torque spanwise distributions due to the presence of the stator, not considered by the model. The cascade-based model demonstrates clear superiority over the Gaussian deficit approach, as it captures the more complex shape of the vane-induced velocity deficit and yields an accurate prediction of the time-averaged upwash velocity field at the rotor trailing edge. The comparison between the LBM and RANS time-averaged fields suggests that, as expected, a periodic RANS simulation provides a reasonable approximation of the flow quantities required for tonal noise prediction, particularly for the dominant interaction components, while maintaining a substantially reduced computational cost. These results indicate that the proposed low-fidelity reconstruction approach can reproduce the dominant characteristics of the time-averaged flow field while drastically reducing computational cost, making it suitable for rapid aeroacoustic assessments and design-space exploration.

The introduction of the modified chordwise pressure distribution function improves the agreement with acoustic trends and eliminates the leading edge singularity typical of the flat plate assumption. However, an overestimate in $c_{p,rms}$ persists and leads to overprediction of blade loading harmonics.

The cascade-based and RANS-based approach captures the dominant tonal trends and reproduce the overall directivity behavior with reasonable agreement relative to the LBM reference, particularly at lower harmonics where the most energetic interaction components are observed. Moreover, they capture the impact of relative blade-vane phasing, predicting with good accuracy the tonal SPL variation between configurations. The Gaussian-based model, instead, does not show satisfactory results mainly due to the limited shape that the velocity field can assume in that case.

Some of the discrepancies still present are due to the lack of a broadband noise model, the presence of turbulent tip flow noise due to flow separation on the blade pressure side, and the breaking of the low-frequency approximation at higher frequencies. These aspects will be addressed in future works. Overall, the proposed framework offers a low-cost and physically interpretable method for early-stage aeroacoustic design and optimisation of engine cooling modules in installed conditions.

CRediT authorship contribution statement

Francesco Bellelli: Writing – original draft, Visualization, Validation, Methodology, Investigation, Formal analysis, Data curation, Conceptualization; **Renzo Arina:** Writing – review & editing, Supervision, Resources; **Stéphane Moreau:** Writing – review & editing, Supervision, Resources; **Francesco Avallone:** Writing – review & editing, Supervision, Resources.

Declaration of competing interest

The authors declare that they have no known competing financial interests or personal relationships that could have appeared to influence the work reported in this paper.

Data availability

The data that has been used is confidential.

Appendix A. Sears function corrections

The corrections adopted in the present work extend the original Sears transfer function to account for compressibility effects, blade incidence, and blade camber. These models are derived within the framework of linearized or weakly nonlinear thin airfoil theory and therefore assume small perturbations of the mean flow, attached flow conditions, and small gust amplitudes.

The compressibility correction proposed by Amiet [43] is valid for subsonic flows and becomes increasingly relevant at moderate Mach numbers and high reduced frequencies. The term $S_\beta(\sigma_\theta)$ in Eq. (6) is

$$S_\beta(\sigma_\theta) = \frac{S_0(\sigma_\theta)}{\beta}\left[J_0\left(\frac{M^2\sigma_\theta}{\beta^2}\right) + iJ_1\left(\frac{M^2\sigma_\theta}{\beta^2}\right)\right]\exp\left(-i\frac{\sigma_\theta f_\beta(M)}{\beta^2}\right), \tag{A.1}$$

where $\beta = \sqrt{1-M^2}$ and $f_\beta(M) = (1-\beta)\log(M) + \sqrt{\beta}\log(1+\sqrt{\beta}) - \log(2)$. $S_0(\sigma_\theta)$ is the original Sears' transfer function reported in Eq. (5).

The angle of attack and camber corrections, proposed respectively by Goldstein [44] and Atassi [45], are second order corrections accounting for the distortion of the incoming gust by the steady potential flow around the airfoil. These corrections are formally valid for thin airfoils with small incidence and camber and become increasingly important at moderate and high reduced frequencies, where the interaction between steady and unsteady perturbations is no longer negligible. It is worth to remind that the corrections listed in Eqs. (A.2) and (A.7) are independent respectively to the angle of attack and to the blade camber, as specified in Eq. (6).

The blade angle of attack term $S_\alpha(\sigma_\theta)$ in Eq. (6) is

$$\begin{aligned} S_\alpha(\sigma_\theta) = &\frac{\Re(\kappa)}{|\kappa|}\left[\frac{-4\Re(\kappa)\Im(\kappa)}{|\kappa|^2}S(\kappa) + \Theta_+\left(\frac{\kappa}{2}\right) - \Theta_-^*\left(\frac{\kappa}{2}\right)\right] \\ &+ iC(\Re(\kappa))\left[\Lambda_+\left(\frac{\kappa}{2}\right) - \Lambda_-^*\left(\frac{\kappa}{2}\right)\right], \end{aligned} \tag{A.2}$$

where $\kappa = \sigma_\theta + i\sigma_\theta/w$,

$$C(x) = iH_1(x)/(H_0(x) + iH_1(x)), \tag{A.3}$$

$$\Theta_\pm(x) = i\pi x \frac{J_1(x)\Im\left[H_\pm(x)J_\pm^*(x)\right] - J_\pm^*(x)}{J_\pm(x)}, \tag{A.4}$$

$$J_\pm(x) = J_0(x) \pm iJ_1(x), \tag{A.5}$$

and

$$\Lambda_\pm(x) = \pm i\pi x^2 \Im\left[H_\pm(x)J_\pm^*(x)\right]. \tag{A.6}$$

The blade camber term $S_c(\sigma_\theta)$ in Eq. (6) is

$$\begin{aligned} S_c(\sigma_\theta) = &\frac{4}{|\kappa|}\left\{-i\Re(\kappa)\left[8\Im(\kappa)\frac{\left(\Re(\kappa)^2 - \Im(\kappa)^2\right)}{|\kappa|^4}\right]P(\kappa)\right. \\ &+ 4\Re(\kappa)\frac{\Im(\kappa)}{|\kappa|^2}\left[\pi\Re(\kappa)G\left(\frac{\kappa}{2}\right) - E(\kappa)\right] \\ &\left.+ C(\Re(\kappa))\left[F_+\left(\frac{\kappa}{2}\right) - F_-^*\left(\frac{\kappa}{2}\right)\right]\right\} \end{aligned} \tag{A.7}$$

where

$$P(x) = \frac{2}{\pi\Re(x)H_+(\Re(x))}, \tag{A.8}$$

$$F_\pm(x) = \frac{x}{x^*}\frac{\pi x J_\pm(x)\Im\left[\left(H_1(x)J_1(x)\right)^*\right] - J_1^*(x)}{J_1(x)}, \tag{A.9}$$

and

$$E(x) = \Re(x)J_2(x) + C(x)\left[\Re(x)J_+(x) - J_1(x)\right]. \tag{A.10}$$

$\Re(x)$ and $\Im(x)$ are respectively the real and imaginary part of x, while x^* is the complex conjugate of x.

Appendix B. On the application of a cascade-based model

The benefits of using a cascade-based approach rather than an isolated airfoil solution in the analytical reconstruction of the time-averaged flow field at the blade trailing edge are hereby discussed.

Fig. B.1 shows the axial velocity with respect to the inflow velocity for a NACA 0012 airfoil at angle of attack $\alpha = 10°$ and for a twist angle $\gamma = 0$, sampled at a distance $s/c = 0.1$ from the leading edge for both the isolated case and the cascade with different values of the inter-blade spacing d/c. The maximum value $d/c = 4$ has been chosen to be representative of the vane spacing of the EB/EV configuration and also the values of s/c, α, and γ are representative of the present configuration. Even at the largest d/c, the cascade configuration differs noticeably from the isolated airfoil solution. The presence of neighboring airfoils induces a redistribution of the induced velocity field that cannot be captured otherwise. The axial velocity profile becomes progressively more symmetric about $y/c = 0$ as d/c decreases, and its magnitude and curvature differ from the isolated solution across the whole y/c. These differences persist even when d/c is sufficiently large that one might intuitively expect the airfoil to behave independently.

This behavior confirms that the cascade formulation adopted in Section 3.4 provides a more physically consistent representation of the vane-induced potential field for configurations such as the ones investigated here. Therefore, a cascade-based model remains an appropriate choice for reconstructing the time-averaged flow field at the blade trailing edge, even for relatively large inter-blade spacings.

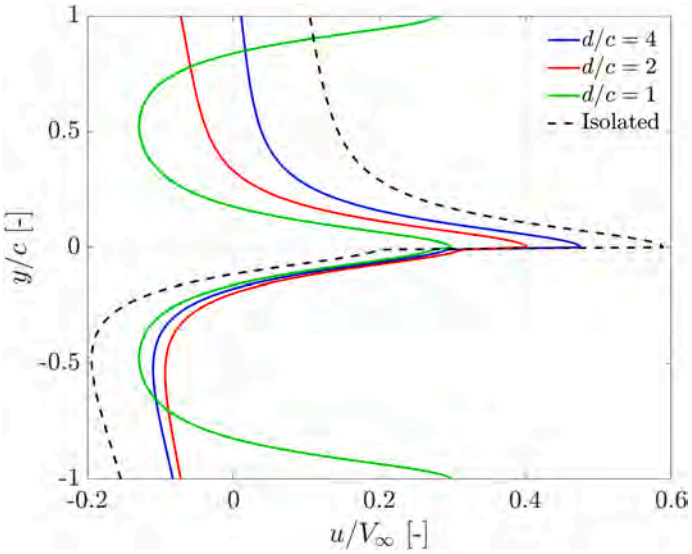


Fig. B.1. Axial velocity profile for a NACA 0012 airfoil with $\gamma = 0$, at $\alpha = 10°$ sampled at $s/c = 0.1$ from the leading edge.

C. Convergence study on N_s and N_c

Fig. C.1 shows, for different number of spanwise points N_s and chordwise points N_c, the SPL in dB at the BPF, its first two harmonics, and the OASPL in the frequency range $0 \leq f/BPF \leq 4$ computed for a probe located at $r_1/D = 2.15$ and $\varphi = 0°$ (along the rotational axis). The EB/EV configuration is shown in Fig. C.1a while the UB/UV configuration is shown in Fig. C.1b. The model has been fed with the flow field obtained using the "Potential" approach. Both the EB/EV and UB/UV configurations indicate that, regardless of the frequency, more points in the spanwise direction than in the chordwise direction are required to reach convergence. Moreover, it is seen a slower convergence for the UB/UV configuration (Fig. C.1b) with respect to the EB/EV configuration (Fig. C.1a). This is particularly evident at $f/\Omega = 3B$ while it is less pronounced at the other frequencies.

The values $N_s = 10$ and $N_c = 20$ were selected as a compromise between accuracy and computational cost. In particular, they correspond to the smallest discretization levels for which the variations of the SPL at the BPF, its first two harmonics, and the OASPL become sufficiently small for the present analysis (less than 5 dB). Although small residual changes remain visible in Fig. C.1, further refinement beyond these values leads only to marginal modifications of the acoustic levels, while significantly increasing the computational effort.

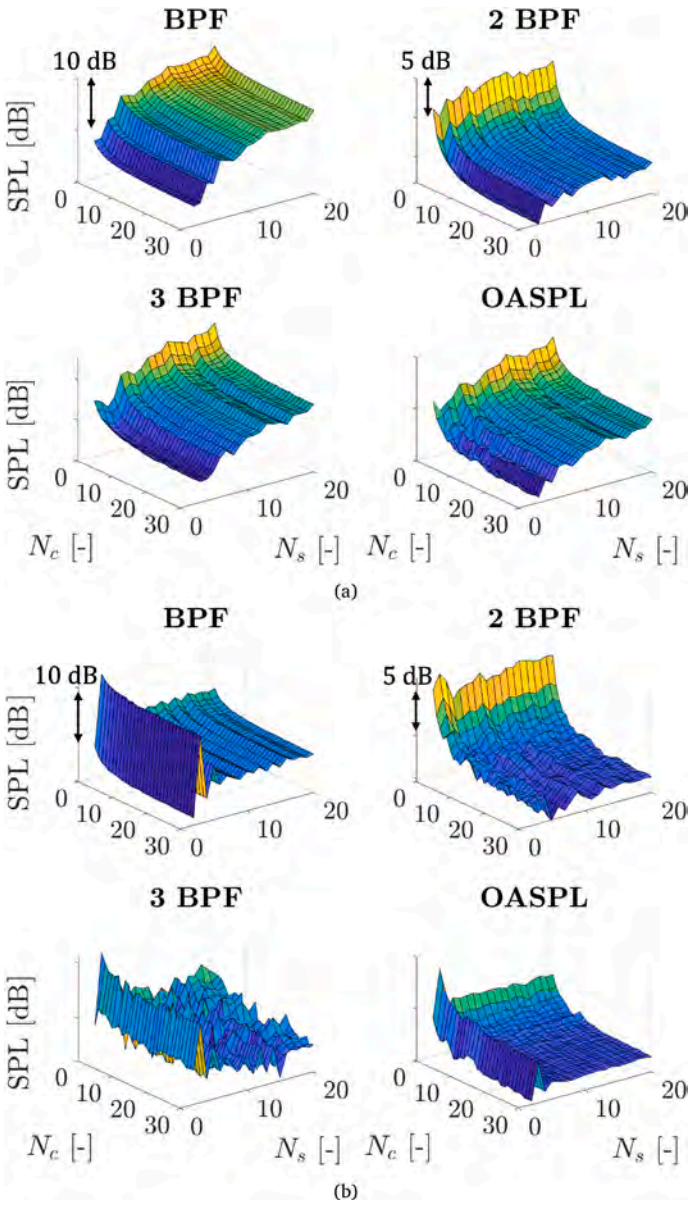


Fig. C.1. Convergence trend of the SPL in dB at $f/\Omega = B$ (BPF), $f/\Omega = 2B$ (2 BPF), $f/\Omega = 3B$ (3 BPF), and the OASPL for a probe located at $r_1/D = 2.15$ and $\varphi = 0°$ (along the rotational axis). (a): EB/EV. (b): UB/UV.

Appendix D. On the benefits of the pressure distribution function modification

The benefits of modifying the pressure distribution function $f(x_1^*)$, as described in Section 3, are hereby discussed.

Fig. D.1 shows the $\Delta c_p = c_{p,PS} - c_{p,SS}$ chordwise distribution on a rotor blade at $R/R_t = 0.75$ both sampled from the LBM simulations and computed with Sears' model by integrating in the frequency range $0 \leq f/BPF \leq 4$ the integrand of the double integral in Eq. (4). The rms values of Δc_p obtained from the LBM simulations and computed with the analytical model using both $f(x_1^*)$ (termed $\Delta c_{p,orig}^{Model}$) and $f_m(x_1^*)$ (termed $\Delta c_{p,mod}^{Model}$) are reported. Moreover, it is also reported the time-averaged value of Δc_p obtained from the LBM simulations to compare it with the corresponding rms value. Indeed, both the averaged and rms Δc_p distributions sampled from the LBM simulation show a peak at the same x_1^* location, slightly past the leading edge, consistently with what reported in [68]. This allows defining the parameter B in Eq. (8) by looking at the average c_p, readily obtainable from XFOIL. The dominant loading in the leading edge region results from the large receptivity of the blade leading edge. Therefore, the aerodynamic response remains strongly weighted toward the leading edge, while the pressure jump tends to zero at the trailing edge consistently with the Kutta condition. The average Δc_p distribution shows important deviations from the rms for $x_1^* \geq -0.75$ due to the flow separation on the

pressure side. The original $f(x_1^*)$ distribution shows a singularity at the leading edge which is regularized by the modified $f_m(x_1^*)$. The latter can also correctly predict the peak value of $\Delta c_{p,rms}$ of the LBM simulation. However, both the original and modified pressure distribution functions tend to overestimate the $\Delta c_{p,rms}$ on the whole chord, with the modified $f_m(x_1^*)$ showing slightly higher values than the original $f(x_1^*)$ due to the constraint of its integration in $x_1^* \in [-1, 1]$.

Fig. D.2 shows the SPL difference between the UB/UV and EB/EV configurations for a far-field probe located at $r_1/D = 2.15$ and $\varphi = 0°$ considering $f(x_1^*)$ and $f_m(x_1^*)$. The use of $f_m(x_1^*)$ is seen to lead to a slightly better match of the analytical model calculations with respect to the reference simulations.

Therefore the proposed modification $f_m(x_1^*)$ is beneficial to the model and has been used throughout the paper.

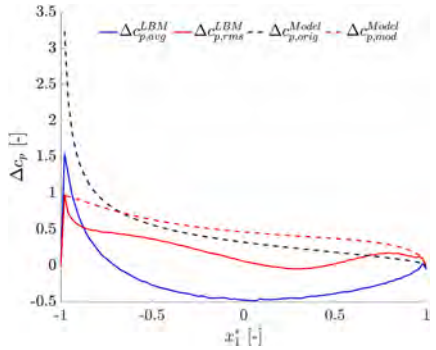


Fig. D.1. Chordwise distribution of Δc_p sampled from the LBM and calculated with Sears' model at $R/R_t = 0.75$ on a rotor blade.

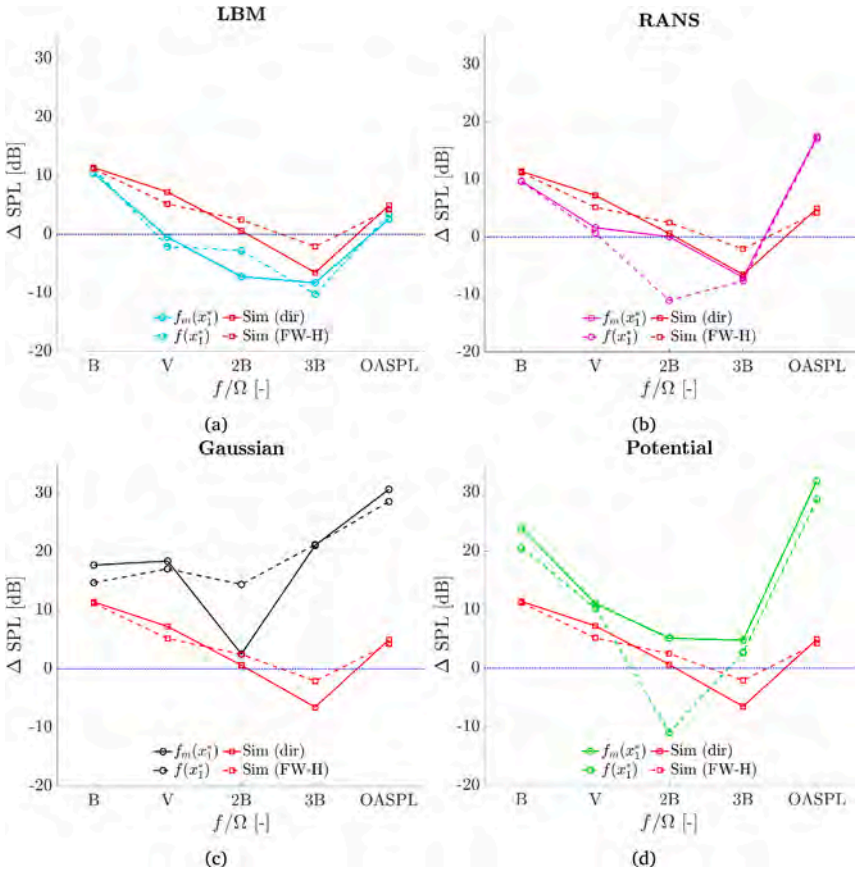


Fig. D.2. SPL difference between the UB/UV and EB/EV configurations for a far-field probe located at $r_1/D = 2.15$ and $\varphi = 0°$. (a): LBM. (b): RANS. (c): Gaussian. (d): Potential.

References

[1] S. Moreau, M. Roger, Advanced noise modeling for future propulsion systems, Int. J. Aeroacoust. 17 (6–8) (2018) 576–599. https://doi.org/10.1177/1475472X18789005
[2] I. Sharland, Sources of noise in axial flow fans, J. Sound Vib. 1 (3) (1964) 302–322.
[3] L. Gutin, On the Sound Field of a Rotating Propeller, NACA-TM-1195 Physikalische Zeitschrift der Sowjetinion: Physical magazine of the Soviet Union volume 9 1 Vol. 9 (1948).
[4] M. Lowson, Theoretical analysis of compressor noise, J. Acoust. Soc. Am. 47 (1970) 371–385.
[5] M. Lowson, The sound field for singularities in motion, Proc. R. Soc. London Ser. A Math. Phys. Sci. 286 (1965) 559–572.
[6] D.B. Hanson, Helicoidal surface theory for harmonic noise of propellers in the far field, AIAA J. 18 (10) (1980) 1213–1220. https://doi.org/10.2514/3.50873
[7] D.B. Hanson, Influence of propeller design parameters on far-field harmonic noise in forward flight, AIAA J. 18 (11) (1980) 1313–1319. https://doi.org/10.2514/3.50887
[8] D.B. Hanson, Compressible helicoidal surface theory for propeller aerodynamics and noise, AIAA J. 21 (6) (1983) 881–889. https://doi.org/10.2514/3.60132
[9] D.B. Hanson, Noise of counter-rotation propellers, J. Aircr. 22 (7) (1985) 609–617. https://doi.org/10.2514/3.45173
[10] W.K. Blake, Mechanics of Flow-Induced Sound and Vibration Volume 2: Complex Flow-Structure Interactions, Elsevier, 2017. https://doi.org/10.1016/B978-0-12-809274-3.00007-6
[11] Y. Wu, M.J. Kingan, S.T. Go, Propeller–strut interaction tone noise, Phys. Fluids 34 (5) (2022) 055116.
[12] M. Sanjosé, S. Moreau, Fast and accurate analytical modeling of broadband noise for a low-speed fan, J. Acoust. Soc. Am. 143 (5) (2018) 3103–3113. https://doi.org/10.1121/1.5038265
[13] R.K. Amiet, Noise Produced by Turbulent Flow Into a Rotor: Theory Manual for Noise Calculation, National Aeronautics and Space Administration, Langley Research Center, 1989.
[14] S. Sinayoko, M. Kingan, A. Agarwal, On the effect of acceleration on trailing edge noise radiation from rotating blades, in: 19th AIAA/CEAS Aeroacoustics Conference, American Institute of Aeronautics and Astronautics, Berlin, Germany, 2013. https://doi.org/10.2514/6.2013-2287
[15] S. Sinayoko, M. Kingan, A. Agarwal, Trailing edge noise theory for rotating blades in uniform flow, Proc. R. Soc. A: Math. Phys. Eng. Sci. 469 (2157) (2013) 20130065. https://doi.org/10.1098/rspa.2013.0065
[16] M. Dieste, G. Gabard, Random particle methods applied to broadband fan interaction noise, J. Comput. Phys. 231 (24) (2012) 8133–8151.
[17] Y. Wu, D. Pan, Z. Peng, H. Ouyang, Blade force model for calculating the axial noise of fans with unevenly spaced blades, Appl. Acoust. 146 (2019) 429–436. https://doi.org/10.1016/j.apacoust.2018.11.008
[18] V. Daydé-Thomas, C. Polacsek, X. Gloerfelt, M. Sugiyama, J. Mardjono, Tone noise prediction of an open-fan engine using a source-mode integral formulation, in: 10th Convention of the European Acoustics Association Forum Acusticum, European Acoustics Association, Turin, Italy, 2023, pp. 3873–3880. https://doi.org/10.61782/fa.2023.0467
[19] J. Rendon, A. Arroyo Ramo, S. Moreau, M. Roger, A numerical and analytical approach of the sound-scattering effects in rotor-strut interaction noise of small-size drones, in: 30th AIAA/CEAS Aeroacoustics Conference, American Institute of Aeronautics and Astronautics, 2024. https://doi.org/10.2514/6.2024-3047
[20] E. Tannoury, S. Khelladi, B. Demory, M. Henner, F. Bakir, Influence of blade compactness and segmentation strategy on tonal noise prediction of an automotive engine cooling fan, Appl. Acoust. 74 (5) (2013) 782–787. https://doi.org/10.1016/j.apacoust.2012.11.015
[21] S. Caro, S. Moreau, Aeroacoustic modelling of low pressure axial flow fans, in: 6th Aeroacoustics Conference and Exhibit, American Institute of Aeronautics and Astronautics, Lahaina, HI, U.S.A., 2000. https://doi.org/10.2514/6.2000-2094
[22] W.R. Sears, Some aspects of non-stationary airfoil theory and its practical application, J. Aeronaut. Sci. 8 (3) (1941) 104–108. https://doi.org/10.2514/8.10655
[23] F. Yunus, D. Casalino, G. Romani, M. Snellen, Efficient prediction of propeller noise in non-axial uniform inflow conditions, Aerosp. Sci. Technol. 157 (2025) 109860. https://doi.org/10.1016/j.ast.2024.109860
[24] N. Van Arnhem, R. De Vries, T. Sinnige, R. Vos, G. Eitelberg, L.L.M. Veldhuis, Engineering method to estimate the blade loading of propellers in nonuniform flow, AIAA J. 58 (12) (2020) 5332–5346. https://doi.org/10.2514/1.J059485
[25] L. Soulat, I. Kernemp, M. Sanjose, S. Moreau, R. Fernando, Numerical assessment of the tonal noise of counter-rotating open rotors at approach, Int. J. Aeroacoust. 15 (1–2) (2016) 23–40. https://doi.org/10.1177/1475472X16630861
[26] S. Guerin, A. Moreau, C. Menzel, C. Weckmueller, Open-rotor noise prediction with a RANS-informed analytical method, in: 18th AIAA/CEAS Aeroacoustics Conference, American Institute of Aeronautics and Astronautics, 2012. https://doi.org/10.2514/6.2012-2303
[27] G. Grasso, S. Moreau, J. Christophe, C. Schram, Multi-disciplinary optimization of a contra-rotating fan, Int. J. Aeroacoust. 17 (6–8) (2018) 655–686. https://doi.org/10.1177/1475472X18789000
[28] E. Canepa, A. Cattanei, F. Mazzocut Zecchin, Effect of the rotor–stator gap variation on the tonal noise generated by axial-flow fans, Appl. Acoust. 94 (2015) 29–38. https://doi.org/10.1016/j.apacoust.2015.01.015
[29] E. Vella, R. Gojon, H. Parisot-Dupuis, N. Doué, T. Jardin, M. Roger, Mutual interaction noise in rotor-beam configuration, in: 30th AIAA/CEAS Aeroacoustics Conference, American Institute of Aeronautics and Astronautics, 2024. https://doi.org/10.2514/6.2024-3318
[30] E. Vella, R. Gojon, H. Parisot-Dupuis, N. Doué, T. Jardin, M. Roger, Mutual interaction noise in rotor–beam configuration, AIAA J. 64 (5) (2026) 2795–2810.
[31] R. Zamponi, A. Beni, A. Zarri, J. Christophe, Prediction of potential interaction noise in a generic rotor–strut arrangement, J. Sound Vib. (2026) 119805.
[32] M. Sanjose, M. Pestana, S. Moreau, M. Roger, Influence and modeling of OGV heterogeneity, in: 22nd AIAA/CEAS Aeroacoustics Conference, American Institute of Aeronautics and Astronautics, Lyon, France, 2016. https://doi.org/10.2514/6.2016-2881
[33] M. Sanjosé, S. Moreau, M. Pestana, M. Roger, Effect of weak outlet-guide-vane heterogeneity on rotor–stator tonal noise, AIAA J. 55 (10) (2017) 3440–3457. https://doi.org/10.2514/1.J055525
[34] A.B. Parry, Theoretical Prediction of Counter-Rotating Propeller Noise, Ph.D. thesis, University of Leeds, 1988.
[35] M. Roger, S. Moreau, A. Guédel, Vortex-shedding noise and potential-interaction noise modeling by a reversed sears' problem, in: 12th AIAA/CEAS Aeroacoustics Conference (27th AIAA Aeroacoustics Conference), 2006, p. 2607.
[36] R. He, M.J. Kingan, X. Wang, X. Kong, H. Zhu, Multi-Rotor unmanned aerial vehicle rotor-strut interaction tonal noise, Appl. Acoust. 242 (2026) 111054.
[37] F. Bellelli, R. Arina, S. Moreau, F. Avallone, Analytical model for predicting rotor-stator interaction tonal noise in low-speed axial fans, in: InterNoise 2025, 2025.
[38] F. Bellelli, R. Arina, F. Avallone, On the impact of operating condition and testing environment on the noise sources in an industrial engine cooling fan, Appl. Acoust. 227 (2025) 110252. https://doi.org/10.1016/j.apacoust.2024.110252
[39] A. Cattanei, F. Mazzocut Zecchin, A. Di Pasquali, A. Lazari, Effect of the uneven blade spacing on the noise annoyance of axial-flow fans and side channel blowers, Appl. Acoust. 177 (2021) 107924. https://doi.org/10.1016/j.apacoust.2021.107924
[40] W. Shao, J. Li, Review of lattice Boltzmann method applied to computational aeroacoustics, Arch. Acoust. (2023). https://doi.org/10.24425/aoa.2019.128486
[41] M. Drela, XFOIL: an analysis and design system for low Reynolds number airfoils, in: Low Reynolds Number Aerodynamics, 1989.
[42] J.F. Manwell, J.G. McGowan, A.L. Rogers, Wind Energy Explained: Theory, Design and Application, John Wiley & Sons, 2010.
[43] R.K. Amiet, Compressibility effects in unsteady thin-airfoil theory, AIAA J. 12 (2) (1974) 252–255. https://doi.org/10.2514/3.49212
[44] M.E. Goldstein, H. Atassi, A complete second-order theory for the unsteady flow about an airfoil due to a periodic gust, J. Fluid Mech. 74 (4) (1976) 741–765. https://doi.org/10.1017/S0022112076002036
[45] H.M. Atassi, The sears problem for a lifting airfoil revisited - new results, J. Fluid Mech. 141 (1984) 109–122. https://doi.org/10.1017/S0022112084000768
[46] M. Roger, A. Carazo, Blade-geometry considerations in analytical gust-airfoil interaction noise models, in: 16th AIAA/CEAS Aeroacoustics Conference, American Institute of Aeronautics and Astronautics, Stockholm, Sweden, 2010. https://doi.org/10.2514/6.2010-3799
[47] N. Joukowsky, Über die konturen der tragflächen der drachenflieger, Z. für Flugtech. Mot. 1 (22) (1910) 281–285.

[48] P.J. Baddoo, L.J. Ayton, Potential flow through a cascade of aerofoils: direct and inverse problems, Proc. R. Soc. A: Math. Phys. Eng. Sci. 474 (2217) (2018) 20180065. https://doi.org/10.1098/rspa.2018.0065
[49] P. Bloomfield, Fourier Analysis of Time Series: An Introduction, John Wiley & Sons, 2004.
[50] J. Ffowcs Williams, D. Hawkings, Sound generation by turbulence and surfaces in arbitrary motion, Philos. Trans. R. Soc. London Ser. A Math. Phys. Sci. 264 (1151) (1969) 321–342.
[51] X. He, L.-S. Luo, Theory of the lattice Boltzmann method: from the Boltzmann equation to the lattice Boltzmann equation, Phys. Rev. E Stat. Phys. Plasmas Fluids Relat. Interdiscip. Topics 56 (6) (1997) 6811–6817.
[52] H. Chen, S. Kandasamy, S. Orszag, R. Shock, S. Succi, V. Yakhot, Extended Boltzmann kinetic equation for turbulent flows, Science 301 (5633) (2003) 633–636.
[53] C.M. Teixeira, Incorporating turbulence models into the Lattice-Boltzmann method, Int. J. Mod. Phys. C. 09 (08) (1998) 1159–1175.
[54] B. Launder, D. Spalding, The numerical computation of turbulent flows, Comput. Methods Appl. Mech. Eng. 3 (2) (1974) 269–289.
[55] F. Avallone, W. Van Der Velden, D. Ragni, D. Casalino, Noise reduction mechanisms of sawtooth and combed-sawtooth trailing-edge serrations, J. Fluid Mech. 848 (2018) 560–591. https://doi.org/10.1017/jfm.2018.377
[56] F. Bellelli, R. Arina, S. Moreau, F. Avallone, Aeroacoustics analysis of radiator installation effects in a pulling engine cooling module, in: FAN2025 Conference, 2025.
[57] F. Farassat, G.P. Succi, The prediction of helicopter rotor discrete frequency noise, In: American Helicopter Society (1982) 497–507.
[58] P. Welch, The use of fast Fourier transform for the estimation of power spectra: a method based on time averaging over short, modified periodograms, IEEE Trans. Audio Electroacoust. 15 (2) (1967) 70–73.
[59] P.E. Duncan, B. Dawson, Reduction of interaction tones from axial flow fans by suitable design of rotor configuration, J. Sound Vib. 33 (2) (1974) 143–154. https://doi.org/10.1016/S0022-460X(74)80102-1
[60] F. Bellelli, R. Arina, S. Moreau, F. Avallone, Aeroacoustic impact of heat exchanger installation in an industrial engine cooling module, Appl. Acoust. 245 (2026) 111175.
[61] D. Lallier-Daniels, M. Piellard, B. Coutty, S. Moreau, Aeroacoustic study of an axial engine cooling module using lattice-Boltzmann simulations and the Ffowcs Williams and Hawkings' analogy, Eur. J. Mech. - B/Fluids 61 (2017) 244–254. https://doi.org/10.1016/j.euromechflu.2016.10.008
[62] L.F. Richardson, The approximate arithmetical solution by finite differences of physical problems involving differential equations, with an application to the stresses in a masonry dam, Philos. Trans. R. Soc. Lond. 210 (459–470) (1911) 307–357.
[63] R.K. Amiet, High frequency thin-airfoil theory for subsonic flow, AIAA J. 14 (8) (1976) 1076–1082.
[64] S. Caro, Contribution à la prévision du bruit d'origine aérodynamique d'un ventilateur de refroidissement, Ph.D. thesis, Ecully, Ecole centrale de Lyon, 2003.
[65] S. Moreau, D. Casalino, Aeroacoustic design of automotive engine cooling fan systems, in: 11th AIAA/CEAS Aeroacoustics Conference, American Institute of Aeronautics and Astronautics, Monterey, California, 2005. https://doi.org/10.2514/6.2005-2906
[66] D. Casalino, S. Moreau, M. Roger, One, no one and one hundred thousand methods for low-speed fan noise prediction, Int. J. Aeroacoust. 9 (3) (2010) 307–327. https://doi.org/10.1260/1475-472X.9.3.307
[67] J. Lee, K. Cho, S. Lee, Application of acoustic analogy to automotive engine-cooling fan noise prediction, AIAA J. 38 (6) (2000) 1095–1098.
[68] A. Piccolo, R. Zamponi, F. Avallone, D. Ragni, Turbulence distortion and leading-edge noise, Phys. Fluids 36 (12) (2024) 125183.